Superconducting properties of Py/Al structures

Christianne Beekman

Doctoraalscriptie

Superconducting properties of Py/Al structures

Doctoraalscriptie

Christianne Beekman
Natuurkunde
Studentnr.: 9932194

Faculteit der wiskunde en natuurwetenschappen
Huygens laboratorium

Leiden, 2005

Contents

List of Figures

List of Tables

Chapter 1

Introduction

In 1911 superconductivity was discovered. Certain materials undergo a phase transition and exhibit a resistance change from normal resistance to zero resistance when cooled through the superconducting transition temperature, T_c. Macroscopically, the resistance of these materials disappears, becoming a perfect conductor. However, at the origin of this phase transition lies the quantum character of the superconducting state. Superconductivity is a result of the formation of Cooper pairs when the superconductor is cooled through the transition temperature. A microscopic theory describing the behavior of a superconductor was developed by Bardeen, Cooper and Schrieffer (BCS theory)[1] and a phenomenological theory was proposed even before the BCS theory by Ginzburg and Landau[2] (GL theory). The BCS theory provides the tools to calculate the energy gap Δ, if Δ is constant in space. The GL theory, which combines the quantum character of the superconductor with the theory for phase transitions, describes a superconductor with Δ varying in space for T close to T_c.

The driving force behind conventional superconductivity is the phonon mediated electron-electron interaction, responsible for the formation of Cooper pairs. These Cooper pairs are large and "hazy" particles with a spatial extension of ξ_0, the BCS coherence length. This coherence length can vary, for example from 38 nm for niobium to about 2 μm for aluminum. When hybrids of S/X bilayers are fabricated, with X a normal metal or a ferromagnet, these layers exchange phase information, this is called the proximity effect. The "hazy" nature of the Cooper pair is responsible for the proximity effect. One can imagine that a Cooper pair can extend over the interface, reducing the order parameter in S but inducing an order parameter in X. The existence of the energy gap, Δ, in the superconductor induces a scattering process, Andreev reflection, at the S/X interface. When the material which is in contact with the superconductor is ferromagnetic in nature there is a pair-breaking effect on the Cooper pairs in the superconductor. This pair-breaking effect results in a suppression of T_c of the superconductor.

This effect can be used in spintronics devices, such as spin switches. A spin switch consists of a superconducting layer which is sandwiched between two ferromagnetic layers. The superconducting transition temperature of the superconducting layer will be more suppressed when the F layers have a mutual magnetization orientation which is parallel than in the antiparallel orientation. This is caused by the stronger pair-breaking effect in the parallel orientation. A spin switch can basically have two different geometries:

- A "vertical" F/S/F geometry with one of the ferromagnetic layers pinned by an anti-ferromagnetic layer. This device was theoretically proposed by Tagirov[3] and Buzdin[4]. The pinning layer is necessary to ensure different switching fields of the F banks (a wide interval were mutual orientation is antiparallel is needed). A first experiment was done by Gu and Bader [6].

- A lateral F/S/F geometry. A pinning layer is not necessary because different aspect ratios [1] of the F banks can be used to ensure different switching fields. To see any effect in a lateral switch a superconductor with a long coherence length should be used, like aluminum.

The ultimate goal of this graduation project was to explore the feasibility of producing and measuring a lateral spin switch. We want to produce and measure a Py/Al/Py lateral spin switch but, in contrast to Jedema[18] (measured this device with Al in normal state), we want to measure the spin switch with the aluminum going through the superconducting transition until spin transport is inhibited by the formation of Cooper pairs.

Outline of report

An outline of the theory needed to interpret our experiments will be given in **chapter 2**. Among other subjects proximity effect and suppression of T_c in S/F bilayers will be treated. Also spin switches will be briefly discussed.

The experimental setup, the hardware and software interface implemented for transport measurements, the sample preparation: the sputtering process, the lift-off technique and the fabrication of the lateral spin switch is discussed in **chapter 3**. Furthermore, the calibration of the aluminum and permalloy is presented.

The results of the experiments that we performed are shown in **chapter 4** and finally conclusions and suggestions for future research are given in **chapter 5**.

[1] $Aspect\ ratio = \frac{length\ F\ strip}{width\ F\ strip}$

Chapter 2

Theory

2.1 Brief overview of superconductivity

In 1911 Kamerlingh Onnes discovered that in a small temperature range the electrical resistance of several metals (mercury, lead and tin) disappeared. The temperature were this phenomenon occurred differed for various metals indicating that this critical temperature T_c is characteristic of the material. This phenomenon was named superconductivity. The concept of superconductivity has puzzled physicists for decennia. Today there exist several theories describing this phenomenon. These theories exist due to the effort of people like Bardeen, Cooper, Schrieffer, Ginzburg, Landau, Gorkov and many others.

A superconductor cannot be just described as a perfect conductor. Meissner and Ochsenfeld [7] discovered that an externally applied magnetic field is expelled from a superconductor when the temperature decreases through T_c. However a perfect conductor would tend to do exactly the opposite: trapping flux in. Furthermore, there will be a critical magnetic field H_c were superconductivity will be destroyed.

Thus, the characteristics of a superconductor are zero electrical resistance below a temperature T_c and below H_c expulsion of the applied magnetic field. Furthermore, the transition from the normal metal state to the superconducting state is a phase transition.

The London brothers [8] were the first to describe the behavior of superconductivity. They proposed the London equations. Later various physicists established the existence of an energy gap in the density of states (DOS) of the order of $\mathrm{k}_B\mathrm{T}_c$ [9] [10]. After this the BCS theory was produced by Bardeen, Cooper and Schrieffer [1]. Ginzburg and Landau introduced the Ginzburg-Landau (GL) theory [2] and thereby introduced the order parameter ψ, a pseudo wavefunction, which is related to the density of superconducting electrons. Both these theories will be presented in the following sections.

Figure 2.1: The lattice distortion caused by a passing electron.

2.2 Formation of Cooper pairs

A metal can be described as the collective system of a positively charged lattice of ion cores surrounded by a negatively charged electron sea. Since the electrons move much faster than the ions the assumption could be made that the dynamics of the electrons is decoupled from the dynamics of the lattice. However, this does not hold for electrons with energies close to the Fermi energy and mixed dynamics have to be taken into account. These electrons will distort the lattice in their vicinity. This distortion can be seen as a polarization cloud and the electron together with the cloud can be indicated as a quasiparticle.

This electron-lattice interaction causes the ions to move a little, this displacement creates a wave in the lattice, a phonon. In figure 2.1 the electron and the lattice distortion are shown. The distortion of the lattice locally causes an increase in charge density. Other electrons will be attracted by this distortion, in principle introducing an attractive force between the two quasiparticles. So indirectly these electrons exchange virtual phonons (see fig. 2.2). This phonon exchange and thus the attractive interaction is responsible for the formation of Cooper pairs which is the driving force of superconductivity (dissipationless transport). The frequency of the interacting phonon is a measure for the stiffness of the lattice. Electrons within an energy interval $\hbar\omega_D$ around the Fermi energy participate in the interaction, therefore ω_D is a cut-off frequency. The attractive interaction potential is zero outside this interval.

2.3 The BCS theory

Bardeen, Cooper and Schrieffer [1] were the founders of the so called BCS theory (weak coupling theory) which revolutionized our understanding of superconductivity. It is most convenient to write this theory in the language of second quantization, by describing everything in terms of creation ($c^*_{k\uparrow}$)

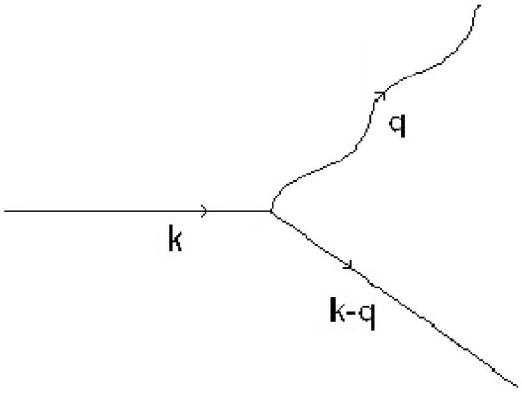

Figure 2.2: Exchange of a phonon with the lattice.

and annihilation operators ($c_{k\uparrow}$). The ground state can be expressed as,

$$|\psi_G >= \prod_{k=k_1,...,k_m} (u_k + v_k c^*_{k\uparrow} c^*_{-k\downarrow})|\Phi_0 > \tag{2.1}$$

with $|\Phi_0 >$ the vacuum state (no particles present), $|u_k|^2$ the probability that a pair state is unoccupied and $|v_k|^2$ that it is occupied. The Hamiltonian that has to be diagonalized is [11],

$$H_{BCS} = \sum_{k,\sigma} (\varepsilon_k - \mu) c^*_{k\sigma} c_{k\sigma} - V \sum_{k,k'} c^*_{k\uparrow} c^*_{-k\downarrow} c_{-k\downarrow} c_{k\uparrow} \tag{2.2}$$

(see also [12]). Here μ, the chemical potential, is more or less equal to the Fermi energy, ε_k is the energy of an electron in state k with $k>k_F$ and V is the pairing potential.

The diagonalized Hamiltonian can be written as

$$H_{BCS} = \sum_k \Big((\varepsilon_k - \mu) - E_k \Big) + \frac{\Delta^2}{V} + \sum_k E_k (\gamma^*_{k0}\gamma_{k0} + \gamma^*_{k1}\gamma_{k1}) \tag{2.3}$$

with

$$\Delta_k = V \sum_k < c_{-k\downarrow} | c_{k\uparrow} > \, , \, E_k = (\Delta_k^2 + \xi_k^2)^{1/2} \text{ with } \xi_k = \varepsilon_k - \mu \tag{2.4}$$

and the Bogoliubov transformations

$$\gamma^*_{k0} = u^*_k c^*_{k\uparrow} - v^*_k c_{-k\downarrow} \tag{2.5}$$

$$\gamma^*_{k1} = u^*_k c^*_{-k\downarrow} + v^*_k c_{k\uparrow} \tag{2.6}$$

The operators γ^*_{k0} and γ^*_{k1} excite a quasiparticle into one of the states of the pair state (k↑,-k↓) leaving the other one unoccupied. This process effectively takes away the possibility for this pair state to participate in the many body wavefunction of the condensate and therefore raises the energy of the system. Therefore the first two terms in the Hamiltonian (eq. 2.2) refer to the ground state and the third refers to excitations. It is immediately evident that the ground state energy is

$$E_G = \Big((\varepsilon_k - \mu) - E_k\Big) + \frac{\Delta^2}{V} \tag{2.7}$$

To determine Δ at T=0 the ground state energy has to be minimized. Differentiating and putting $\delta \mathrm{E}_G/\delta\Delta = 0$ gives,

$$\Delta = \frac{w_D}{sinh(\frac{1}{VN(0)})} \simeq 2\omega_D e^{\frac{-1}{VN(0)}} \tag{2.8}$$

This approximation is valid because we are in the *weak coupling limit* were $VN(0) \ll 1$. Here ω_D is the Debye frequency and N(0) is the electronic density of states at the Fermi energy. Even if the attractive potential is infinitely small, there will still be a finite order parameter (energy gap).

What is the relationship between Δ and the superconducting transition temperature T_c? The gap is largest when T=0 and it decreases with increasing T. At the superconducting transition temperature, T_c the gap will vanish (i.e. Δ=0). Consequently, the system ceases to be superconducting and will go back to the normal state. By minimizing the energy (including the third term of eq. 2.2, which refers to the excitations) and taking $\Delta \rightarrow 0$ as T approaches T_c results in,

$$\beta_c^{-1} \simeq 1.13\omega_D e^{\frac{-1}{VN(0)}} \tag{2.9}$$

with ${\beta_c}^{-1}=k_B T_c$. In the weak coupling case (i.e. weak coupling between electrons and phonons) the ratio of the gap to T_c becomes a universal number,

$$\frac{2\Delta(0)}{k_B T_c} = 3.53 \tag{2.10}$$

This relation holds for superconductors like aluminum.

2.4 The Ginzburg Landau theory

The BCS theory is suited in dealing with an order parameter which is constant in space. However, the microscopic theory becomes very difficult when Δ starts to be inhomogeneous in space (for example: in S/F systems). In this case the Ginzburg Landau theory[2] (GL), a macroscopic theory based on Landau's theory on second order phase transitions, is more convenient.

The GL theory only holds for T close to T_c and introduces the complex order parameter, ψ

$$\psi = |\psi| e^{i\phi} \tag{2.11}$$

Here $|\psi|$ is the amplitude of the order parameter and ϕ contains the phase information. When ψ is varying slowly in space, the free energy density can be expanded in series of ψ [1][13];

$$f = f_{n0} + \alpha|\psi|^2 + \frac{\beta}{2}|\psi|^4 + \frac{1}{2m^*}\left|\left(\frac{\hbar}{i}\nabla - \frac{e^*}{c}\mathbf{A}\right)\psi\right|^2 + \frac{h^2}{8\pi} \tag{2.12}$$

where h is an externally applied field, $f_{n0}+\frac{h^2}{8\pi}$ is the free energy density of the normal state and $\mathbf{A}$ is the vector potential. Here e^* and m^* are the effective charge and the effective mass of a Cooper pair and therefore, e^*=2e and m^*=2m with e and m the electronic charge and mass. The parameters α and β are functions dependent on temperature and the fourth term deals with fields and gradients.

Minimizing f is done by taking δf/$\delta\psi$=0, which results in the well known GL differential equations,

$$\alpha\psi + \beta|\psi|^2\psi - \frac{\hbar^2}{4m}\left(\nabla - \frac{2ie}{\hbar c}\mathbf{A}\right)^2\psi = 0 \tag{2.13}$$

$$\mathbf{j} = \frac{c}{4\pi}\mathrm{curl}\mathbf{h} = -\frac{ie\hbar}{2m}(\psi^*\nabla\psi - \psi\nabla\psi^*) - \frac{2e^2}{mc}\psi^*\psi\mathbf{A} \tag{2.14}$$

Equation 2.13 is very similar to the Schrödinger equation for particles with eigenvalues -α. The second term in the equation can be seen as a repulsive potential. Since this potential of ψ basically acts on itself, the wavefunction $\psi(\mathbf{r})$ tends to spread out throughout space as much as possible.

If there are no external magnetic fields or gradients present ($\mathbf{A}$ and $\nabla\psi$ are zero) the solution to eq. 2.13 with the lowest free energy is given by,

$$|\psi|^2 = -\frac{\alpha}{\beta} \tag{2.15}$$

Close to T_c, β is taken constant and α=$a(T - T_c)$. Furthermore, close to T_c, the amplitude of the order parameter is small. Neglecting terms in eq. 2.13 containing products of $|\psi|$ gives the linearized GL equation,

$$\alpha\psi - \frac{\hbar^2}{4m}\left(\nabla - \frac{2ie}{\hbar c}\mathbf{A}\right)^2\psi = 0 \tag{2.16}$$

When there are no applied magnetic fields ($\mathbf{A}$=0), the second term (eq. 2.16) describes the variation of ψ and therefore it is natural to define a

[1]Since the free energy is real and $\hat{\psi}$ is complex, the expansion is be carried out in powers of$|\psi|^2$

characteristic length for variation of ψ in space, namely the GL coherence length, $\xi(T)$,

$$\xi_{GL}^2(T) = \frac{\hbar^2}{4m|\alpha(T)|} \tag{2.17}$$

Near T_c the following equations for ξ hold,

$$\xi_{GL}(T) = 0.74\frac{\xi_0}{(1-\frac{T}{T_c})^{1/2}} \qquad clean : l \gg \xi_0 \tag{2.18}$$

$$\xi_{GL}(T) = 0.855\frac{(\xi_0 l_e)^{1/2}}{(1-\frac{T}{T_c})^{1/2}} \qquad dirty : l \ll \xi_0 \tag{2.19}$$

with l_e the mean free path and ξ_0=$\hbar v_F/\pi\Delta(0)$ the BCS coherence length, which basically is the spatial extension of the Cooper pair at T = 0. In our case the aluminum is a dirty superconductor and therefore eq. 2.19 must be used.

2.4.1 Type I and type II superconductors.

When a superconducting material is in the normal state a magnetic field can completely penetrate the material. However when the material is cooled through T_c the magnetic field is expelled from the interior of the superconductor. Inside the superconductor the magnetic field decays exponentially to zero. The distance over which the magnetic field has decayed to $\frac{1}{e}B_{ext}$ (with B_{ext} the magnetic field outside the superconductor) is called the penetration depth, λ_L. The penetration depth is given by [14],

$$\lambda_L(T) = \frac{\lambda_L(0)}{|2(1-\frac{T}{T_c})|^{1/2}} \tag{2.20}$$

with $\lambda_L(0)$ the London penetration depth, which is given by

$$\lambda_L(0) = (\frac{mc^2}{4\pi n_s e^2})^{1/2} \tag{2.21}$$

with m, e the electronic mass, c the speed of light and charge and n_s the number density of superconducting electrons (electrons participating in Cooper pair formation). The two characteristic lengths $\xi(T)$ and $\lambda_L(T)$ have similar T-dependence and when T$\rightarrow$T$_c$ both approach infinity. The ratio of these quantities is

$$\kappa = \frac{\lambda_L(T)}{\xi(T)} \tag{2.22}$$

Using equations 2.21 and 2.19 gives

$$\kappa = 0.715\frac{\lambda_L(0)}{l} \qquad dirty : l \ll \xi_0 \tag{2.23}$$

Superconductors can be divided into two groups based upon their different response to magnetic fields: type I and type II superconductors. In type I superconductors superconductivity is destroyed at a certain critical field H_c while type II superconductors go into an intermediate state at H_{c1} where normal state channels (vortices) coexist with the superconducting state. This intermediate inhomogeneous superconducting state is destroyed at a second critical field H_{c2} leaving the system in the normal state. When $\kappa < \frac{1}{\sqrt{2}}$ the superconductor is type I and when $\kappa > \frac{1}{\sqrt{2}}$ it is of type II.

2.5 Ferromagnetism

In contrast to non-magnetic materials, ferromagnets have a spontaneous magnetic moment (in zero field). The spin direction of the electrons is not randomized but ordered and this ordering induces an internal field, the *exchange field*. However, thermal energy competes with this ordering trying to randomize the spin direction and at a certain temperature the thermal energy destroys the ordering completely. This destruction happens at the Curie temperature T_C [2]. When all spins are pointing in the same direction, i.e. there is uniform magnetization throughout the material, the ferromagnet is saturated. Usually this saturation can only be reached by application of an external magnetic field. In zero field the material will be divided in regions with different spin direction called domains. Inside the domains there is uniform magnetization.

Domain walls

During the magnetization process domains are formed which are separated by walls. Mainly, the walls are either Bloch walls or Néel walls.

- Bloch walls: Consider two adjacent domains with opposite direction of magnetization. The wall connects these domains and thus contains spins which rotate from one direction to the opposite direction. In the case of a Bloch wall the rotation is out of the plane of the magnetization direction of the domains.

- Néel walls: Consider again these two domains (again opposite direction of magnetization) but this time separated by a Néel wall. In this case the spins inside the wall rotate in plane instead of out of plane.

Creating Bloch walls costs energy since inside the walls the spins are directed away from the direction of easy magnetization i.e. the anisotropy energy increases. However, their formation also lowers the magnetostatic

[2] $T > T_C$: disordered paramagnetic phase.
$T < T_C$: ordered ferromagnetic phase.

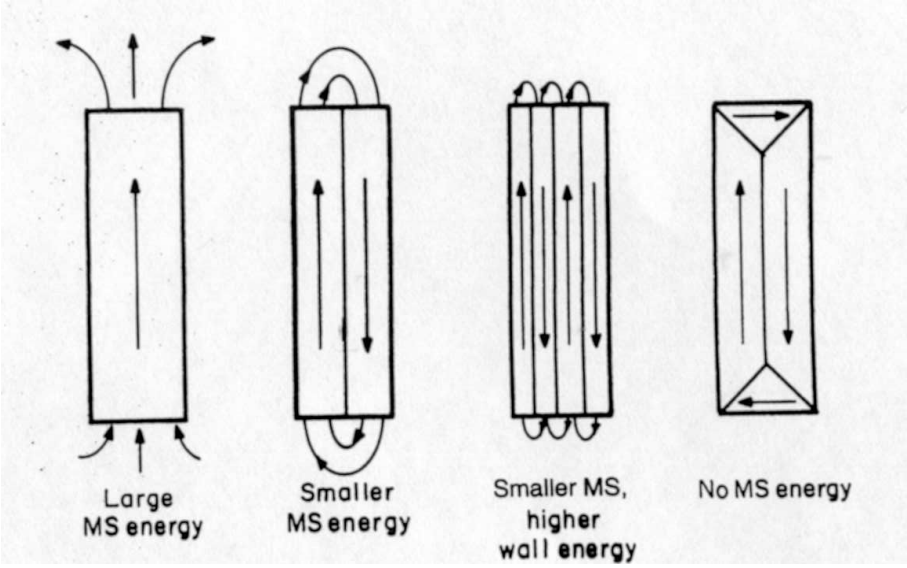

Figure 2.3: Effect of domain formation on magnetostatic energy.

energy (introduced by a discontinuous normal component of magnetization across an interface). If the ferromagnet is saturated i.e. single domain, the magnetostatic energy (MS energy) is large. Creating domain walls lowers the magnetostatic energy as shown in fig. 2.3. However, formation of closure domains is necessary to reduce the MS energy completely to zero. When the thickness of the ferromagnet is reduced the magnetostatic energy will increase. Because of the out of plane rotation in the Bloch wall the wall will, at some point, extend throughout the whole thickness of the ferromagnet, introducing two charged surfaces (see fig.2.4). Moving these surfaces closer together increases the magnetostatic energy. Below a certain thickness, in plane rotation inside the wall will be energetically more favorable than out of plane rotation. The Bloch walls will become Néel walls. Now the charged surfaces are inside the film, however, the area of these charged surfaces decreases with decreasing thickness.

Shape anisotropy

A system always tends towards the state with lowest possible energy. In the case of a long and narrow strip, this means finding the balance between creating domain walls (which costs energy) and minimizing magnetostatic energy. In such a strip it is therefore energetically more favorable to have the magnetization parallel to the long axis of the strip, shape anisotropy. It only causes a magnetostatic field at the far edges of the strip which can be minimized by the formation of closure domains. When the aspect ratio of the strip is large, the strip is effectively single domain. However, there will

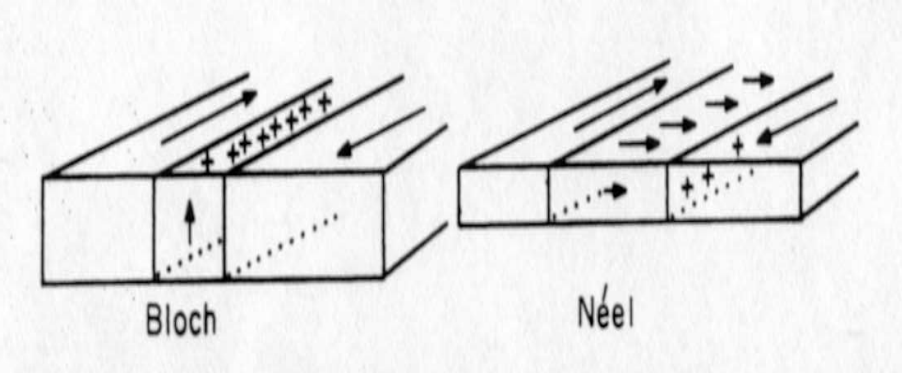

Figure 2.4: Bloch and Néel domain wall extending throughout the whole thickness of the film.

be two closure domains at the far edges of the strip.

Coercivity

Application of an external magnetic field alters the direction of magnetization.

- Weak field: Domains with their magnetization in the same direction as the applied field will grow (this is energetically more favorable). The other domains will shrink and ultimately vanish. This is accomplished by domain wall motion.
- Strong field: In this case the spins which are not aligned with the field direction will rotate until they are parallel to the applied field.

When the field direction is perpendicular to the direction of easy magnetization the spins will rotate towards the field direction quasi statically when the field is increased. If the field is parallel to the easy axis domain wall motion governs the change of the magnetization direction. When the material is in a single domain state the magnetization tends to remain in the same direction even when the field changes sign. At a certain field the energy becomes so large that the magnetization switches abruptly to align with the field direction. Therefore, there is hysteresis in the M-H loops of ferromagnetic materials. A hysteresis loop is shown in fig. 2.5 and the coercivity field is indicated. The coercivity field is defined as the field that has to be applied, to reduce the magnetization M of a sample back to zero, after it has been completely magnetized (M_s).

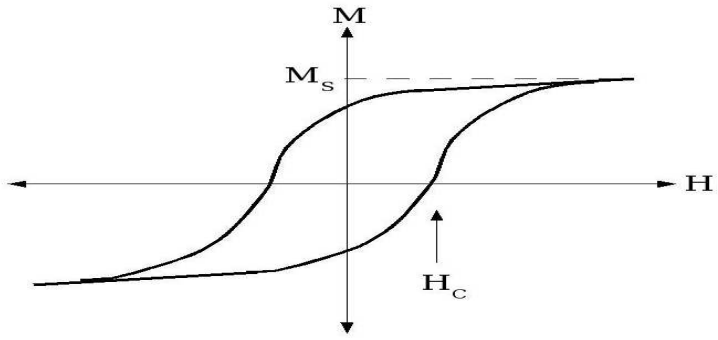

Figure 2.5: Hysteresis loop with the coercivity field H_c indicated.

2.6 Proximity effect

What happens when a superconductor is in contact with another material? The exchange of phase information between the superconductor and the other material is called the *proximity effect*.

2.6.1 Superconductor/Normal metal interface.

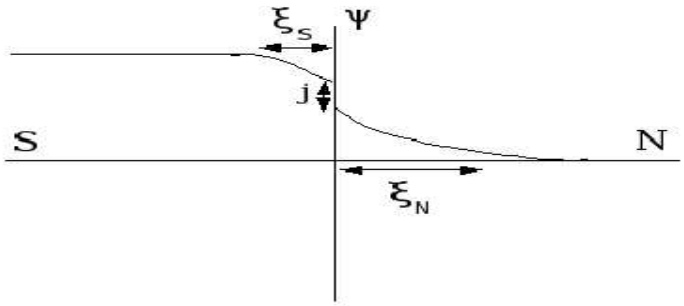

Figure 2.6: Proximity effect at a S/N interface.

The proximity effect in a superconductor-normal metal interface is shown in figure 2.6. The spatial extension of the Cooper pairs induces a finite order parameter in the normal metal. The Cooper pairs can extend over the S/N interface and the part in the normal metal will still feel the pairing force of the superconductor, which not only induces a finite order parameter in the normal metal but also reduces the order parameter in the superconductor (see fig. 2.6). The reduction of the order parameter in the superconductor extends over a length scale of the order of the superconducting coherence

length, ξ_s. The jump of the order parameter at the interface (j) is caused by a finite interface resistance. Interface resistance is a result of scattering processes occurring at the interface, such as scattering on impurities. When there are no external fields applied the following equation holds at the S/N interface,

$$-i\hbar\nabla\Psi = i\frac{\hbar}{\xi_N}\Psi \tag{2.24}$$

So the order parameter will become,

$$\Psi(r) = \Psi_0 e^{-\xi_N r} \tag{2.25}$$

Thus, the order parameter decays exponentially with increasing distance into the normal metal over a distance ξ_N (fig. 2.6).

2.6.2 Andreev reflections

The *proximity effect* is caused by phase coherence between electrons in the superconductor and those in the adjacent material for instance a normal metal. This exchange of phase information is driven by scattering of electrons at the interface: Andreev reflection[15]. When the system is in equilibrium one only has to take into account energies which lie below the energy gap, Δ. There are in principle two processes which can occur at the interface (for $\epsilon < \Delta$), the so called

- Specular reflection: the incoming electron (coming from the normal metal) is completely reflected back into the normal metal as an electron.

- *Andreev reflection*: The incoming electron has an energy below Δ (energy gap in DOS of superconductor) and therefore there are no available energy levels in the superconductor. The electron collides with the interface and is scattered back as a hole. The hole has opposite spin direction compared to the incoming electron and therefore spin is conserved during Andreev reflection. Energy is also conserved since the electron has an energy ϵ above the Fermi surface while the hole has an energy ϵ below the Fermi surface. However, during this process charge is not conserved in the normal metal. A Cooper pair is formed at the interface (the incoming electron takes an electron from below the Fermi surface to form a Cooper pair and is transmitted into the superconductor, leaving a hole in the normal metal). When the hole propagates back along the same path as the incoming electron their phases will be correlated inducing a finite pair amplitude in the normal metal. The induced order parameter decreases exponentially into the normal metal because of dephasing of the electron and hole of the Cooper pair. When the excitation energy of the incoming electron

is ϵ above the Fermi energy the hole will travel on a slightly different path than the incoming electron but they will still be phase correlated to a certain extend.

2.6.3 Superconductor/Ferromagnet interface.

When a superconductor is brought into contact with a ferromagnet the proximity effect is even more evident. A ferromagnet is a so called pair breaker because superconductivity and magnetism are two competing phenomena. Andreev reflection also occurs at the interface in a S/F system but the exchange field has a large influence on the amount of Andreev reflection. When the exchange field is large, Andreev reflection will be suppressed. This can be understood when looking at the rotation symmetry of the spins. In a normal metal all spin directions are equivalent; however, in a ferromagnet there is a majority and a minority spin band (the spin bands are separated by the exchange energy). A spin up electron is Andreev reflected into a spin down hole so the spin has to move from the majority spin band to the minority spin band. Depending on the density of states in both bands a certain amount of electrons ($N_\downarrow/N_\uparrow$ with N the electronic density of states) will be Andreev reflected.

When the Cooper pairs diffuse into the ferromagnet there is an exchange field with a pair-breaking effect on the Cooper pairs. As the Cooper pair moves into the ferromagnet the spins will be subjected to different forces. The spin up electron lowers its potential energy by h (=exchange field energy) and therefore has an increase of kinetic energy. Similarly, the spin down electron raises its potential energy and lowers its kinetic energy[3]. Because of this energy change the momentum of the Cooper pair changes upon entry in the ferromagnet. The center of mass momentum will change with,

$$Q = \frac{2h}{v_F} \tag{2.26}$$

As a consequence, the order parameter will still decrease exponentially but there is an oscillation superimposed on this decay (see fig. 2.7).

However, in this thesis we are mainly interested in what happens in the superconductor. The superconducting transition temperature is suppressed by the exchange field of the ferromagnet, because not only do the Cooper pairs leak into the ferromagnet, but their extension over a coherence length also leads to a lowering of the order parameter in the superconducting layer. The suppression of T_c can be approximated by using the GL theory, which will be explained in the next section.

[3]The change in potential energy must be compensated by change in the kinetic energy because energy must be conserved.

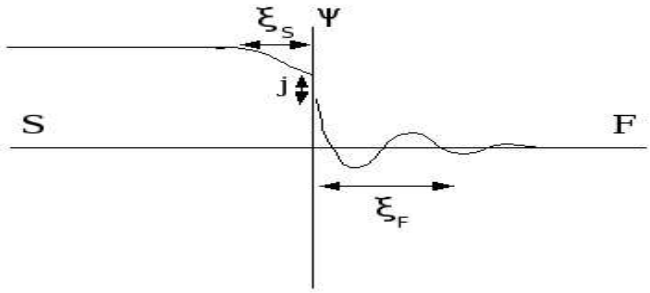

Figure 2.7: Proximity effect at a S/F interface.

2.7 Suppression of T_c.

The behavior of a bulk superconductor is somewhat different from that of a superconducting thin film. When the thickness of the superconductor is decreased to around ξ boundary effects become more important.These boundary conditions for a thin superconducting film are,

$$\left.\frac{\delta\psi(z)}{\delta z}\right|_{z=\pm\frac{d}{2}} = 0 \tag{2.27}$$

meaning that there is no current flowing out of the superconductor. The linearized GL equation 2.16 can be solved using the boundary conditions (eq. 2.27) and a trial solution of the form,

$$\hat{\psi} = \psi(z)e^{(ik_x x + ik_y y)} \tag{2.28}$$

with $\psi(z)$ the amplitude of the complex order parameter varying with z (see fig. 2.8).

Imagine a superconducting thin film sandwiched between to ferromagnetic layers. In this configuration the linearized GL equation can be used with the trial solution 2.28 as in the case of the superconducting thin film. However, the boundary conditions are different,

$$\left.\psi(z)\right|_{z=\pm\frac{d}{2}} = 0 \tag{2.29}$$

When no external magnetic field is present ($\mathbf{A}$=0) and the trial solution mentioned above is used, the linearized GL equation becomes,

$$\frac{-\hbar^2}{4m}\frac{\delta^2\psi}{\delta z^2} + \alpha\psi = 0 \tag{2.30}$$

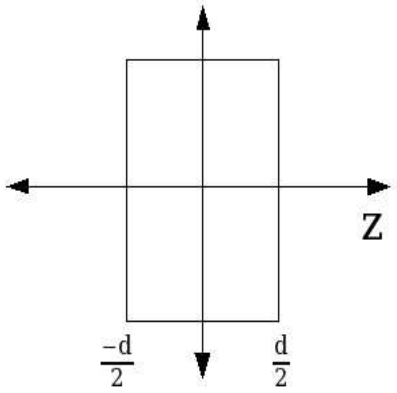

Figure 2.8: Superconducting thin film.

This equation is readily solved and gives,

$$\psi(z) = \psi_0 cos(kz) \quad \text{with} \quad k^2 = -\frac{\alpha 4m}{\hbar^2} \tag{2.31}$$

with $kd = \pi$ for the ground state. For the ground state,

$$-\alpha = \frac{\hbar^2 \pi^2}{4md^2} \tag{2.32}$$

with d the thickness of the superconducting layer. Using the temperature dependence of α (see section 2.4) the suppression of T_c of the superconducting film (due to the presence of the ferromagnetic banks) can be written as,

$$T_c = T_{c0} - \frac{\hbar^2 \pi^2}{4mad^2} \quad \text{with} \quad \alpha = a(T_c - T) \tag{2.33}$$

or

$$T_c = T_{c0} - \frac{\pi^2 \xi_{GL}^2}{d^2} \tag{2.34}$$

Where T_{c0} is the bulk superconducting transition temperature. The transition temperature of the F/S/F trilayer is inversely dependent on d^2. However, when the superconducting layer is thinner than d_{cr}, the critical thickness, superconductivity will be destroyed completely by the exchange fields of the ferromagnets.

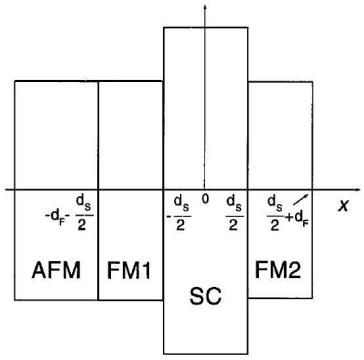

Figure 2.9: The device, proposed by Tagirov.

2.8 Superconducting spin switches

2.8.1 Buzdin, Tagirov, Gu and Bader.

The suppression of the transition temperature caused by the proximity of a ferromagnet can be used in spintronic devices, such as a superconducting spin switch. The spin switch was theoretically proposed by Tagirov[3] and Buzdin[4]. Tagirov proposed a structure (fig. 2.9) where the superconducting layer is sandwiched between two ferromagnetic layers. The magnetization direction of one of the F layers is pinned by the presence of an antiferromagnetic layer while the direction of the second F layer remains free to rotate. The T_c of such a device can be controlled by the exchange fields of the F layers, when the thickness of the superconductor (d_s) is of the order of the superconducting coherence length ξ_s. The Cooper pairs are to probe the spin directions of both F banks at the same time. In this case the exchange field can be used to control T_c. The exchange field can be altered by changing the mutual orientation of the magnetization directions of the F layers. This can be seen by looking at the electrons which leak into the superconductor. These electrons are spin polarized and will reside in states near the Fermi energy. However, the attractive interaction, leading to the formation of Cooper pairs, takes place in these states.Imagine electrons with the same spin direction entering the superconductor[4]. They do not participate in the formation of Cooper pairs. However, since these electrons occupy states near the Fermi energy, these states will become unavailable for the Cooper pair formation process and less Cooper pairs are formed. When electrons with opposite spin direction leak in[5], Cooper pairs can form. As a result the order parameter (and thus T_c) is suppressed more in the Parallel (P) state and much less in the Antiparallel (AP) state. Ide-

[4]Mutual orientation of the exchange fields of the F banks is parallel.
[5]Mutual orientation of the exchange fields of the F banks is antiparallel.

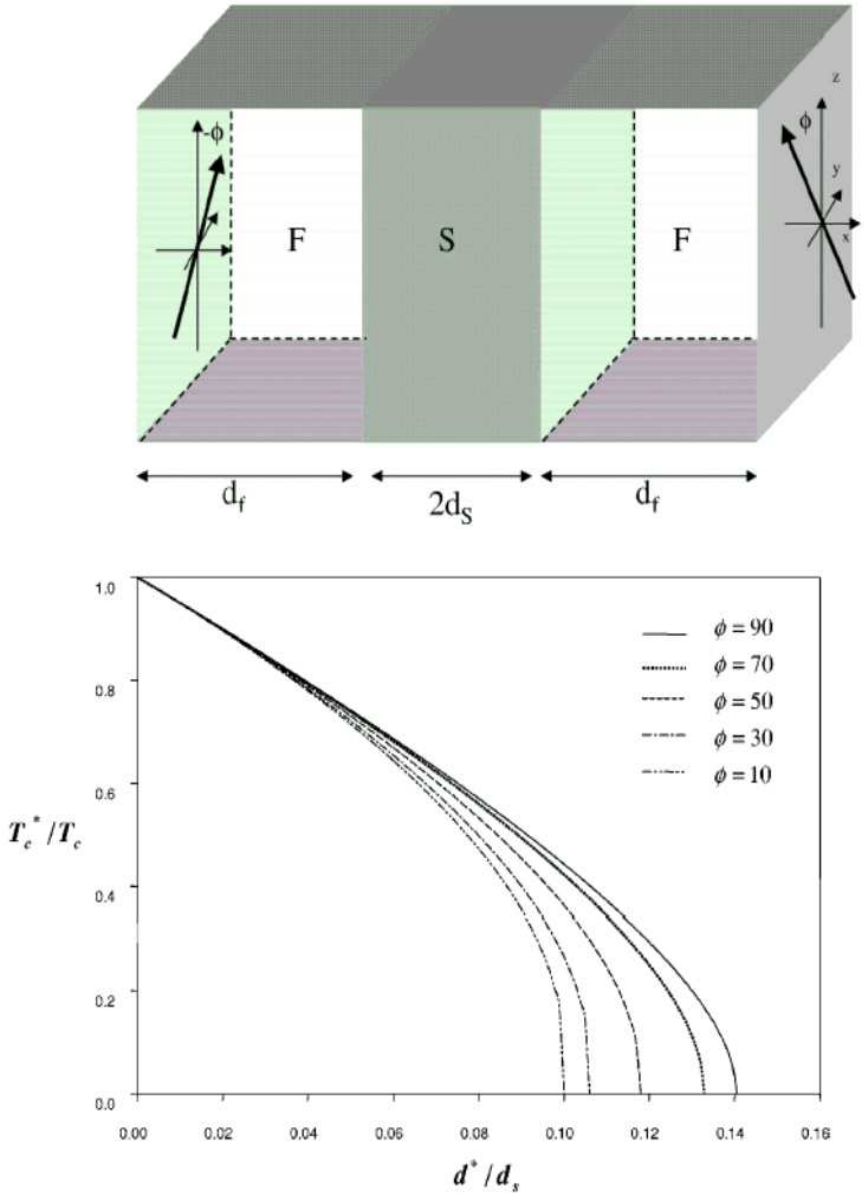

Figure 2.10: Top: superconducting spin switch (F/S/F), the exchange field is given by large arrows and Φ is the angle between the exchange field and the z-axis. Bottom: the suppression of T_c as function of d^*/d_S.

ally when switching form P to AP state one can switch from normal state resistance to zero resistance. Baladié et al[5] calculated the suppression of T_c for the superconducting spin switch which is shown in fig. 2.10. Here ϕ is the angle between the exchange field and the z-axis. In the figure, T_c^*/T_c is given as function of d^*/d_S, where T_c is the transition temperature of a single superconducting layer, T_c^* is the suppressed transition temperature of a F/S/F trilayer, $2d_S$ is the tickness of the superconducting layer and d^* is the effective length,

$$d^* = \gamma\sqrt{\frac{I}{D_F}}\frac{D_S}{4\pi T_c} \tag{2.35}$$

with I the exchange field, γ the interface transparency[6] and D_F and D_S are diffusion coefficients in the ferromagnet and the superconductor. The effective length d^* is proportional to the exchange field I and therefore becomes larger for increasing exchange fields. From the figure it becomes clear that for a certain range of exchange fields the superconductivity is completely destroyed in the P case but only weakly suppressed in the AP case. When $d_{cr}^{AP} > d_S > d_{cr}^{P}$ (with $2d_{cr}$ critical thickness of S), it is possible to go from normal state resistance of S to zero resistance by changing the mutual orientation of the exchange fields of the F banks from parallel to antiparallel orientation.

This effect has been the subject of the experimental research of Gu et al [6]. They measured the effect in the structure shown in figure 2.11 The

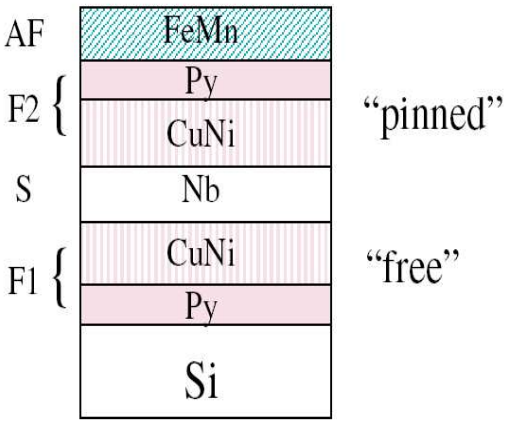

Figure 2.11: The device which was measured by Gu and Bader.

dimensions of the device which they measured are:

- FeMn: thickness = 6 nm

[6] $\gamma = 0$: interface not transparent.
$\gamma = 1$: interface fully transparent.

- Py ($Ni_{82}Fe_{18}$): thickness = 4 nm
- $Cu_{0.47}Ni_{0.53}$: thickness = 5 nm
- Nb: thickness = 18 nm
- $Cu_{0.47}Ni_{0.53}$: thickness = 5 nm
- Py ($Ni_{82}Fe_{18}$): thickness = 4 nm

The layers were deposited on a silicon substrate. The critical thickness, d_{cr}, of Nb in a $Cu_{0.48}Ni_{0.52}$/Nb/$Cu_{0.48}Ni_{0.52}$ trilayer is 14 nm [16]. The composition of the CuNi of Gu and Bader is comparable to the composition used in [16] and it is stated that the critical thickness of Nb is approximately the same for every measured concentration of Ni.

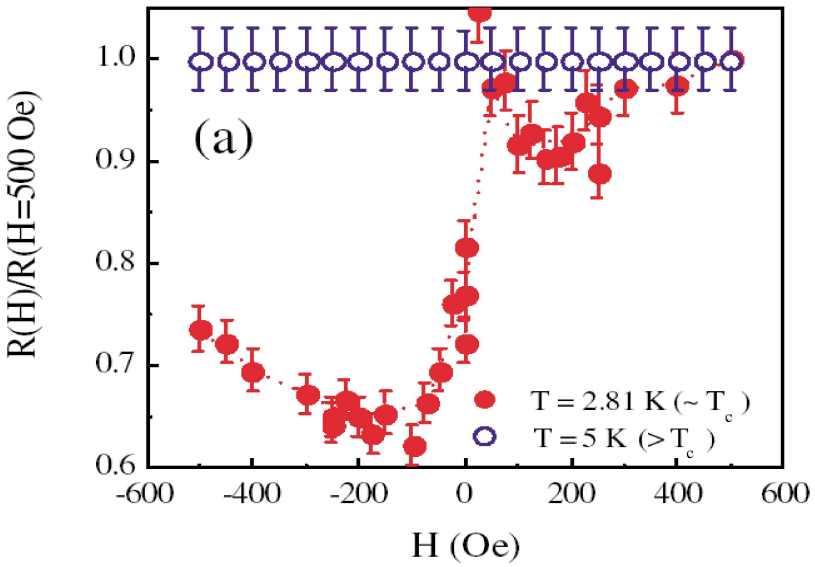

Figure 2.12: Resistance vs. applied magnetic field H. Blue symbols: T=5 K($>T_c$). Red symbols: T=2.81 K($\sim T_c$).

The results of their measurement are depicted in figures 2.12 and 2.13. Figure 2.12 shows no change in resistance when switching from P to AP state for a temperature above the superconducting transition temperature. However, near T_c the figure shows only a $\sim$25% decrease in resistance going from the P to the AP state. The suppression of T_c for the P state compared to the AP state is shown in figure 2.13. Figure 2.13 shows that the shift in T_c is only 6 mK and this shift is much smaller than the width of the transition. This explains the fact that the resistance in figure 2.12 does not drop completely to zero.

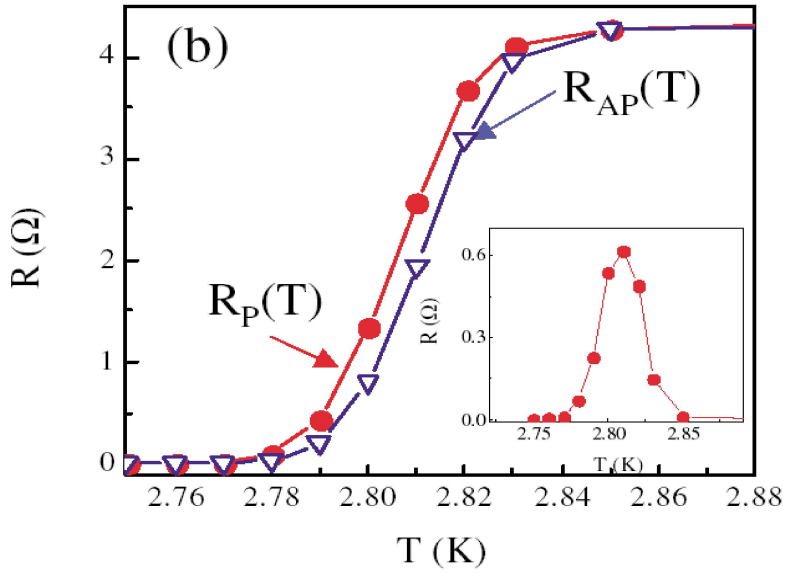

Figure 2.13: Resistance vs. temperature. Inset: difference in resistance between P and AP state vs. temperature.

However, other explanations are possible. For example, the suppression of T_c due to effects caused by the multi domain structure of the ferromagnet[17]. In this case the Cooper pairs also probe multiple directions of magnetization (different directions on either side of the domain wall) which causes the same effect as in the spin switch.

2.8.2 Lateral spin switch.

We want to measure a lateral spin switch. The structure of the device is shown in figure 2.14. Gu et al used an S layer of Niobium in their spin

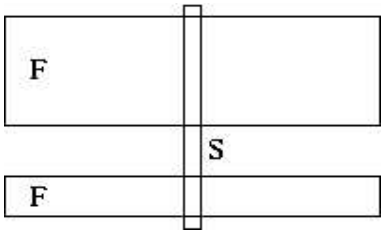

Figure 2.14: The lateral spin device.

switch which has the following characteristic length scales,

$$\xi_0 = 38 \text{ nm} \quad \text{and} \quad \xi_{GL}(0) = 12 \text{ nm} \tag{2.36}$$

As mentioned before the BCS coherence length, ξ_0 is a measure for the spatial extension of Cooper pair and ξ_{GL} is the Ginzburg-Landau coherence length. Therefore Nb is excellent for usage in a spin switch such as the device proposed by Tagirov. However, for a lateral spin switch a much longer coherence length is needed. The spacing between the F banks in our lateral switch has to be more than an order of magnitude larger than the thickness of the S layer used in the device of Gu et al (18 nm); because spacings smaller than 500 nm become very difficult to fabricate. Consequently we chose aluminum as superconductor in the lateral device, since Al has the following characteristic values,

$$\xi_0 \approx 1 - 2\ \mu\text{m} \quad \text{and} \quad \xi_{GL}(0) \approx 200\ \text{nm} \tag{2.37}$$

and a T_c around 1.2 K. We expect that Al has a coherence length which is long enough for a lateral device, which is tested by measuring the Al/Py bilayers. Because of the low T_c of aluminum the devices are measured in a He^3 cryostat.

Jedema[18] performed spin injection measurements on a Py/Al/Py lateral device with Al in the normal state. The ferromagnets are used to inject a current of spin polarized quasiparticles into the adjacent material (Al). In a normal metal quasiparticles with different spin directions have identical conductivities. However, in the ferromagnet spin-up and spin-down quasiparticles have different conductivities. Because of the conductivity difference in F and the conductivity "mismatch" between F and N, spin accumulates near the F/N interface. Because of the diffusive behavior of the quasiparticles in N and F the accumulation (spin polarization) decays with distance from the interface. The characteristic length scales over which this decay occurs is the relaxation length, λ_N and λ_F for normal metal and ferromagnet respectively. When the device in consideration has a electrode spacing L, which is much larger than λ_N, the decay is exponential with L. When $\lambda_F > L > \lambda_N$ the decay of the spin accumulation has a 1/L dependence. Jedema measured the resistance difference between parallel and antiparallel configuration of the F electrodes. The results of their measurements are shown in figure 2.15. In the graph the resistance difference, ΔR between P and AP configuration of the electrodes is shown versus the electrode spacing, L. The squares are the results of a measurement at T=4.2 K and the circles are the result of a measurement at T= 293 K. The squares at L=250 nm and L=500 nm deviate considerably from the remainder of the curve. This deviation was attributed to the granular character of the aluminum (grains with sizes comparable to the width of the Al strip). We used this measurement to determine which dimensions our device should have and still have a reasonable resistance difference. However, we want to measure the device going through the superconducting transition of Al. The amount of spin polarized quasiparticles in the Al will decrease with decreasing temperature until spin transport is inhibited when the Al becomes superconducting.

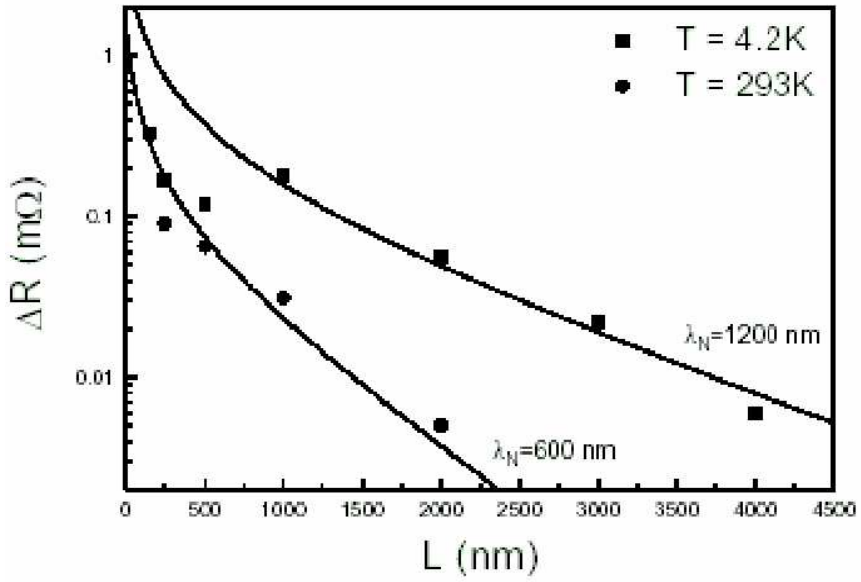

Figure 2.15: The difference in resistance between the P and AP state of a lateral Py/Al/Py lateral spin valve. The spin relaxation lengths, obtained from the fits, are also given.

Chapter 3

Experimental setup

3.1 ^{3}He cryostat

To characterize the Al films and the Al/Py bilayers a ^{3}He cryostat (in our case an Oxford Instruments Helios) is needed because the transition temperature of aluminum is around 1.2 K. A sketch of the insert is shown in figure 3.1. The insert is used in a ^{4}He storage dewer. This cryostat is capable

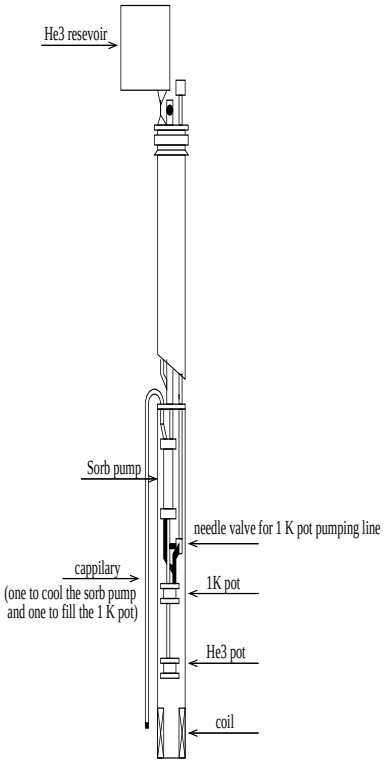

Figure 3.1: Schematic drawing of the ^{3}He insert.

of reaching a base temperature of 300 mK by lowering the vapor pressure of a bath of liquid ^{3}He (^{3}He-pot) by means of a cryogenic sorption pump (sorb pump). The ^{3}He is condensed[1] in the 1K-pot shown in figure 3.1. The system is implemented such that the temperature can be varied between 300 mK and 2.5 K. Temperature stability within 1 mK is achieved for several hours. It is possible to perform AC and DC transport measurements.

3.2 Electronics

In this section several devices used for measuring the samples and controlling the temperature will be explained. Four point measurements are necessary in order to avoid measuring the resistance of the wiring inside and outside the cryostat and the contact resistance.

3.2.1 DC measurement

In performing the DC measurements the following devices were used. A Keithley 220 Programmable current source was used to send a DC current through the sample. A Keithley 181 nanovoltmeter was used to measure the voltage at the sample. To measure these I-V characteristics of single Al layers typically currents between 1 nA up to 1 μA were used. This (DC) setup can measure signals down to just below 1 μV.

3.2.2 AC measurement

A LR-700 resistance bridge[2] was used to measure the temperature dependence of the resistance of single layers of aluminum. Also an SR830 lock-in amplifier and a home built AC+DC current source ("Delftse kast") were added to the setup for the measurement of the lateral spin switches.

To perform AC-transport measurements with standard lock-in technique[3] we used a Delftse kast and a lock-in amplifier. The lock-in amplifier has a signal generator giving out a sine wave with certain amplitude and frequency and a DAC which outputs a DC voltage (see fig. 3.2) (for a voltage sweep) (V_{AC}= 10.58 mV(rms), V_{DC}=200 mV and f_{AC}=131.31 Hz). The DAC is

[1] The ^{3}He condenses at temperatures below ~2.7K.

[2] The LR-700 resistance bridge is used to do a four point measurement of the sample, excluding the wiring and contact resistance from the measurement. The bridge sends a fixed AC excitation current through the sample. The current depends on the resistance range (2 mΩ-2 MΩ) and full scale excitation voltage (20 μV-20 mV), which can be set. The excitation current frequency is 15.9 Hz. The settings of the bridge were controlled by software written in LabView.

[3] DC: a signal constant in time.
AC: A signal with a certain frequency and amplitude which is compared to a reference signal (Lock-in technique) to filter out any noise. Usually, a AC-excitation is used together with a DC signal to measure not only an I-V characteristic but also get information about dI/dV.

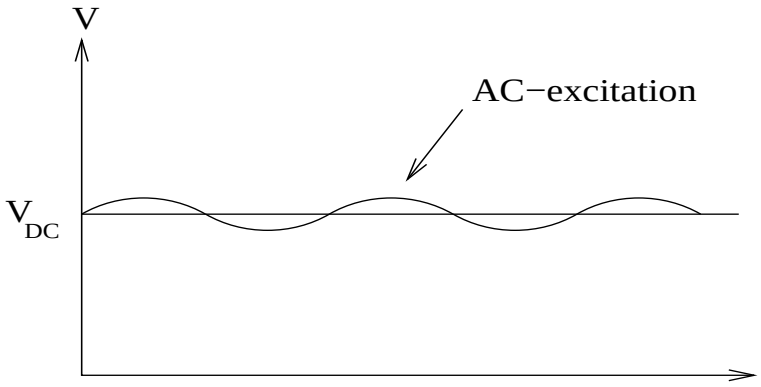

Figure 3.2: A DC voltage is given by the lock-in amplifier together with an AC-excitation. V_{AC}= 10.58 mV(rms), V_{DC}=200 mV and f_{AC}=131.31 Hz.

controlled to give a DC voltage and the sine from the Lock-in amplifier is the excitation voltage. The DC voltage from the DAC and the sine wave are the input[4] for the Delftse kast where both are mixed and converted into current. This current is sent through the sample. The voltage drop over the sample is amplified by the Delftse kast before being measured by the lock-in amplifier. The DC voltage is directly measured by the nanovoltmeter. This DC voltage represents a point on the IV characteristic of the sample and the AC excitation current, going through the sample, induces an oscillation around this point giving information about the derivative $\frac{dI}{dV}$ of the IV characteristic. The excitation voltage which is read is compared to a reference signal, the sine wave. By multiplying the measured AC voltage with the reference wave, the $\frac{dI}{dV}$ is obtained while the noise with random frequency components is filtered out by a low band pass filter. In this way the Lock-in amplifier is capable to measure signals in a noisy background. The Lock-in amplifier settings are controlled by LabView as well as the data acquisition.

3.2.3 Temperature control and external magnetic field

During the resistance vs. temperature measurements, the temperature was controlled with two PID regulation systems:

- by controlling the temperature of the sorption pump (using a Oxford Instruments PID regulator (ITC 503)). This is done for the coarse regulation of the sample temperature.
- by controlling the sample temperature with a heater (1 kΩ) built close to the sample. This is done for fine temperature control and improved temperature stability.

[4] V_{AC} is connected to a 1/100 input in the Delftse kast and V_{DC} is connected to a 1/5 input in the Delftse kast.

The sorb pump temperature is set to a value, such that the ^{3}He-pot temperature is just below the setpoint T_{set}, while the heater is used to approach and maintain the setpoint. The heater output is controlled by a software PID regulator which is written in LabView. As input for the PID controller the resistance of the 2 kΩ RuO_2 thermometer, which was mounted on the sample holder, is measured continously by the LR-bridge. For calibration of the thermometer see Appendix A. The temperature could be held stable within 1 mK for several hours.

Also the application of an external magnetic field is possible. A home made superconducting coil (see Appendix B for calibration) is used to sweep a magnetic field between ±600 Gauss. This coil can produce the fields necessary for the switching of the Py electrodes. The direction of the field (parallel to the axis of the coil) is fixed, but the sample can be mounted perpendicular or parallel to the field direction.

3.3 Sample preparation

In this paragraph the fabrication process of the single Al films, the Al/Py bilayers and the lateral spin switch is explained. Almost all films were sputtered on Si substrates, except the ones which were fabricated for the X-ray measurements (here $SrTiO_3$ (STO) was used).

3.3.1 UHV sputtering system

A UHV (Ultra High Vacuum) system was used to sputter Al and Py layers. The sputtering chamber is constantly evacuated by a turbo pump maintaining a background pressure of about $3{\cdot}10^{-9}$ mbar. The substrates are put into a load lock separated from the chamber, which is pumped down by a second turbo pump. When the pressure is low enough the substrates are transported into the UHV chamber. Inside, layers are deposited by magnetron sputtering.

The sputtering process.

Before sputtering the films argon gas is let into the system. A voltage is applied to the sputtering target, which spontaneously starts to ionize the Ar atoms. Because of the applied voltage the Ar^+ ions are accelerated towards the target. The ions which collide with the target set atoms of target material free. Besides the atoms secondary electrons are formed, ionizing even more Ar atoms and setting more target material free. Dependent on the argon pressure, at some point a stable glow discharge ignites. The sputtered particles are deposited all over the sputtering chamber and therefore also onto a substrate positioned carefully inside the chamber. The ionization efficiency can be enhanced by applying a magnetic field (the magnet is

positioned just behind the target). The applied magnetic field influences the trajectories of the secondary electrons by trapping them in cycloids. In the region near the target the ionization efficiency will increase because of the confinement of the glow discharge. The enhanced ionization has the advantage that the discharge can ignite at lower argon pressures. The mean free path of the atoms is larger at lower pressures, so the atoms collide with the substrate with higher kinetic energy. There are several parameters which influence the properties of the film which is deposited on the substrate. The most important parameters are:

- sputter current: determines the deposition rate of the film. Therefore this parameter determines the time a sputtered particle has to participate in surface diffusion and agglomeration. For the Al layers a sputter current of 220 mA is used and for the Py layer 165 mA is used.

- Ar pressure: as mentioned above the pressure in the chamber determines the mean free path of the target particles approaching the substrate. The distance of the target to the substrate and the pressure determine the number of collisions the target particles encounter on their way to the substrate. This can affect the crystallinity of the film. For Al a pressure of $6.0{\cdot}10^{-3}$ mbar and for Py layers a pressure of $4.0{\cdot}10^{-3}$ mbar was used.

During sputtering the substrate is positioned in the center under the targets. The sample holder can be rotated from an angle of 45 ° (angle between normal to target surface and sample holder plane) and the configuration where the sample holder plane is perpendicular to the normal of the target. For the Py lift-off procedure to succeed the Py layer needs to be sputtered in the perpendicular configuration. This decreases the resputtering against the walls of the bottom layer resist (see section 3.3.3). During sputtering the thickness of the film is monitored by a crystal monitor. The crystal is situated inside the chamber and has a certain resonance frequency (excited by an oscillator). When material is deposited onto the crystal the resonance frequency is shifted. The shift in the resonance frequency is a measure for the amount of material on the crystal. Beforehand parameters like density have to be specified and the crystal monitor needs to be zeroed. When the growth rate of a target is calibrated the thickness of the sample can be determined with the crystal. Growth rates are calibrated with RBS (Rutherford Backscattering Spectroscopy) measurements and X-ray measurements.

3.3.2 Optical lithography

For the transport measurements of single Al and Al/Py layers, where micro-sized structures were needed, we used optical lithography. An optical resist

called HPR 204 was spincoated on top of the Al layer. After baking a few minutes at 90 °C the resist was exposed, with the use of a optical mask, to UV light for 15 seconds. After exposure the sample is put in a developer (AZ 312 MIF) which takes away the exposed resist (positive resist). Normally, after the development an etching step follows, in order to remove the Al which was under the exposed resist. This can be done by wet etching or ion beam etching. In this case we planned to use wet etching with a solution of the following composition 2% HNO_3, 75% H_3PO_4 and 23% H_2O. Surprisingly, this last step was not necessary because the developer already etched away the Al which was underneath the exposed resist. The fabricated structures were strips with the following dimensions: length = 1.4 mm, width = 200 μm and varying thicknesses between 21 nm and 475 nm. Included in the structure are the current and voltage leads and the contact pads for a 4-point measurement.

3.3.3 E-beam lithography

Aluminum with gold contacts

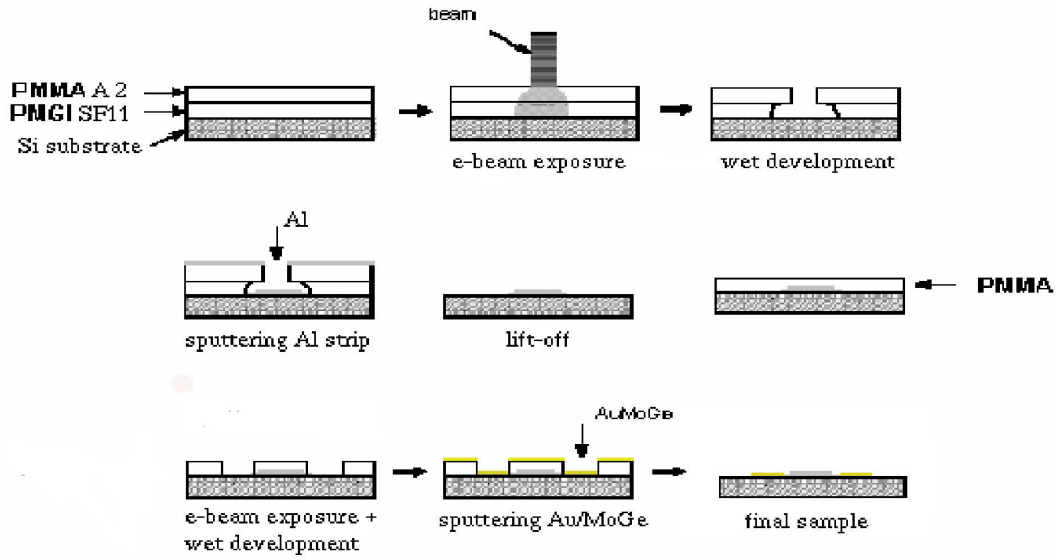

Figure 3.3: The lift-off process.

At first also the Al/Py bilayers were structured with optical lithography. However, the developer (AZ 312 MIF) reacted agressively with the Al. This process caused the destruction of some of the bilayers, making this a highly irreproducible structuring process. So the decision was made to start using e-beam lithography instead. Furthermore, e-beam lithography is required

for fabrication of submicron-sized structures. Since the aim of this work is to study the possibilities of lateral spin switch devices, where sizes between 300 to 1500 nm have to be achieved, we also tested the lift-off fabrication procedure for a single submicron Al-strip. There are two possible structuring processes besides optical lithography which are applicable to our case. The first involving dry etching and the second the lift-off process. Dry etching has the disadvantage that during etching the material which is already etched away is piled up against the resist walls resulting in high edges, "ears". These "ears" are difficult to remove (a possible solution is to etch under different angles or rotate the sample while etching). With the lift-off technique these ears can also form. However, they can be avoided by optimizing the following three parameters of the fabrication process,

- Undercut. In the lift-off technique a bilayer of resist is used. When the top layer of resist has a large overhanging profile compared to the bottom layer (undercut), the resputtering of target particles against the bottom layer resist walls will decrease. Furthermore, a large undercut improves the resolution of the structures significantly.

- The thickness of the bottom layer of resist. When the bottom layer of resist is too thick, more target material is resputtered against the resist walls introducing the so called "ears". So the bottom layer should preferably be as thin as possible. However, when the bottom layer resist is too thin, the sputtered material (in the resist structure) will be attached to the material which is sputtered on top of the resist stack. The structure will be destroyed during the lift-off.

- Ar pressure. Since the Al atoms are quite light a low Ar pressure should be used during sputtering. With a high pressure the atoms are scattered in every direction (also in the undercut) and therefore, the material will pile up against the bottom layer resist walls. One should use the lowest Ar pressure possible (more "directional" sputtering), at which a stable glow discharge can still be ignited.

We chose to apply the lift-off procedure which is depicted in figure 3.3.

First a bilayer of resist was spincoated onto a Si substrate. The bottom layer is PMGI (low resolution resist) and the top one is PMMA (high resolution resist). Both are positive resists[5]. When a single layer of resist is used the achievable resolution is poor. Here sputtered material is piled up against the resist walls. If the resist is thin this pile up causes damage to the structure during lift-off. When a PMMA/PMGI bilayer is used, the (high resolution) PMMA will form a overhanging profile in combination with

[5]Positive resist: during development only the exposed resist is removed. Negative resist: during development only unexposed resist is removed. This definition can depend, for the same resists, on the dose and on the developer.

the undercut PMGI (low resolution) (see fig. 3.3). This will significantly improve the resolution and edge definition of the structure, but not necessarily the "ears". The e-beam writes a structure by exposing this bilayer of resist to an electron beam (typical current: 50 pA). This is followed by development[6] of the resist taking away the exposed parts. The sample is put into the UHV to sputter Al or Py on it by magnetron sputtering. Now the real lift-off can start, after sputtering the sample is put in the NMP[7], which causes the PMGI layer to swell and dissolve. So the whole film will come off except for the part which is sputtered directly onto the substrate, see fig. 3.3. A typical result of this procedure is the Al structure shown in

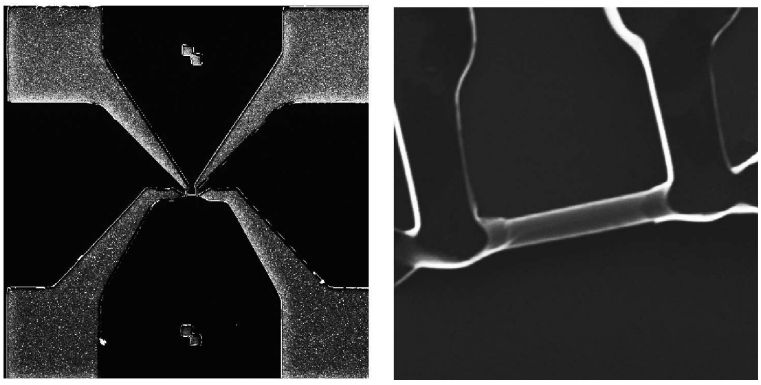

Figure 3.4: Al strip with Au contacts.

fig. 3.4. The dimensions are: length = 5 μm, width = 800 nm and thickness = 42 nm. A second e-beam step is required to make contact pads. Here a single layer of PMMA is sufficient because we do not require a very high resolution. After exposure the Au/MoGe contacts are sputtered in the Z-400. The MoGe layer is an adhesion layer. A final lift off is done with acetone.

3.3.4 Lateral spin switch: The four lithography steps.

The structures in the previous section were used to determine whether the use of the PMMA and PMGI would "pollute" the aluminum and thereby affecting its resistivity and superconducting transition temperature, T_c. The resistance measurements showed that the use of these resists does not influence the characteristic parameters of the Al such as the superconducting transition temperature T_c and its mean free path.

The final goal of this research was to measure a lateral spin switch with the Al in the superconducting transition. The creation of such a device takes four separate writing steps with the e-beam. In figure 3.5 the complete

[6]PMGI: PMGI developer.
PMMA: MIBK:IPA 1:3.

[7]NMP= 1-methyl-2-pyrrolidinone

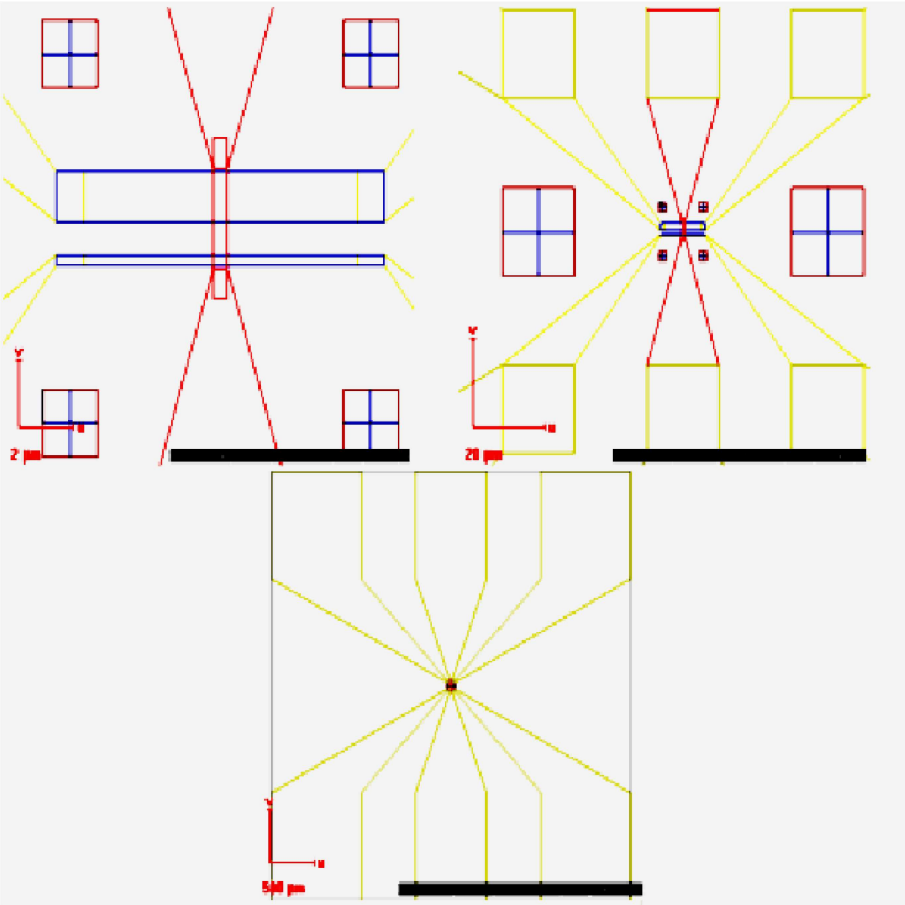

Figure 3.5: Structure designed with e-beam software. Blue structure: Py, red structure: Al and yellow structure: Au.

design of the device is shown. The blue squares are alignment markers to ensure that future writing steps overlap with the previous ones. Such accurate alignments can be done thanks to a computer motorized stage, a beam blanker and software which allows accurate post alignment and stitching.

Py electrodes

The first writing step is to write the Py electrodes. In order to achieve different switching fields for the two Py strips the following dimensions were chosen (see chapter 4, fig. 4.8):

- top electrode :10 μm long and 1.5 μm wide.
- bottom electrode: 10 μm long and 0.3 μm wide.

- thickness: 40 nm
- electrode spacing: 750 nm.

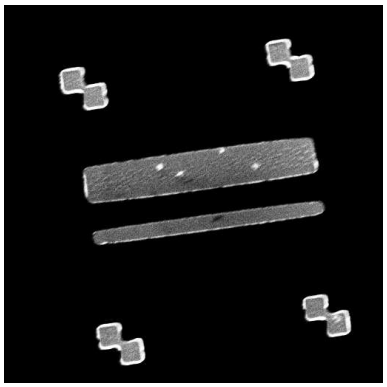

Figure 3.6: Permalloy electrodes.

Figure 3.6 shows the structure after lift-off, the parameters used in the writing and the development are given in Appendix C. From the figure the real sizes can be determined, they are,

- top electrode:10 μm long and 2 μm wide.
- bottom electrode: 10 μm long and 0.75 μm wide.
- thickness: 40 nm
- electrode spacing: 300 nm.

The structures are significantly larger than the sizes aimed for. This is caused by the fact that the Ar pressure was too high during sputtering. When the pressure is high the sputtered atoms are scattered more and they will scatter into the undercut and reduce the resolution. This process also causes the formation of "ears" (AFM studies showed that the "ears" were several hundreds of nanometers high). The argon pressure during sputtering should be decreased to a value even lower than the used 4 μbar.

During sputtering the long axis of the electrodes were aligned with the external magnetic field, caused by the total magnetic field from the magnetron system. Thus, the easy axes of magnetization of the electrodes is directed along the long axis of the electrodes.

Al strip.

The second writing step includes the aluminum strip (red structure) in figure 3.5. The aimed-for size of the strip is (for characteristic values of Al see chapter 4, table 4.1),

- width: 500 nm
- length: 8 μm
- thickness: 80 nm

In figure 3.7 the structure after lift-off is shown, the parameters used in the writing and the development are given in Appendix C. However, the measures in the structure after lift-off are larger than the aimed-for sizes,

- width: 2 μm
- length: 8 μm
- thickness: 80 nm

Also here the pressure during sputtering was too high (6 μ bar), which has decreased the resolution dramatically. For aluminum the effect is larger because the Al atom is lighter than the Ni and Fe atoms. Also one can

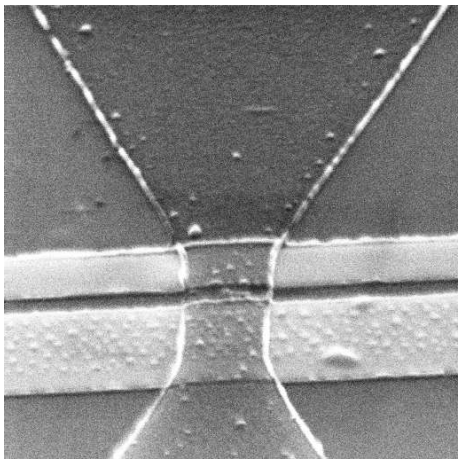

Figure 3.7: Aluminum strip on top of the Py electrodes.

clearly see some ears at the edges of the Al but also on the edges of the Py (damaging the Al because of decreased film thickness in the "shadow" of the "ear"). The bottom layer resist was probably also too thick. However this sample is still measurable.

Au contacts.

Finally two writing steps have to be done to put contacts on the sample for the transport measurements. Both the intermediate and large gold contacts are shown in figure 3.5 as the yellow structures. The intermediate contacts after lift-off are shown in fig. 3.8. The parameters used in the writing and the development are given in Appendix C.

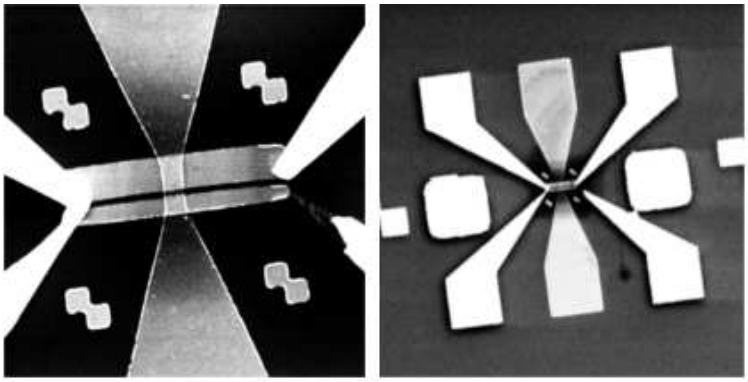

Figure 3.8: Structure with intermediate Au contacts.

The lift-off of the intermediate gold contacts failed, on the left side the top contact was short cutting the bottom contact and at the right side the bottom contact is not overlapping with the Py electrode. This can be explained by the fact that only a single PMMA resist layer was used instead of a bilayer for the fabrication of the Au-intermediate contacts. The shortcut is there because resolution of the resist is higher in a bilayer (PMMA/PMGI) which is apparently necessary for such small structures. (Before a single (PMMA) layer was enough when the structures had larger dimensions.) The damage on the right side was probably caused by underexposure of the smallest structures. The alignment of the gold with the Py is quite good, but it would have been easier and less prone to errors, if the Py electrodes would have had different lengths. Due to such problems, the final measurement could not be performed.

3.4 Calibration of the growth rate of aluminum and permalloy

3.4.1 RBS-measurements

To calibrate the growth rate of Al and Py films Rutherford Backscattering Spectroscopy (RBS) and X-ray measurements were performed. The RBS measurements were performed at AMOLF [8]. This method can be used to measure densities and consequently thicknesses of thin films. Figure 3.9 shows the mechanism of RBS measurements. The thin film is bombarded with light nuclei like α-particles with an energy of 2 MeV. When these particles hit the sample they will be reflected into a detector. The energy of the particles that enter the detector are characteristic of the atom they

[8] AMOLF (Instituut voor Atoom en Molecuul Fysica) is one of the research institutes of F.O.M. (a government institution for Fundamental Research on Matter).

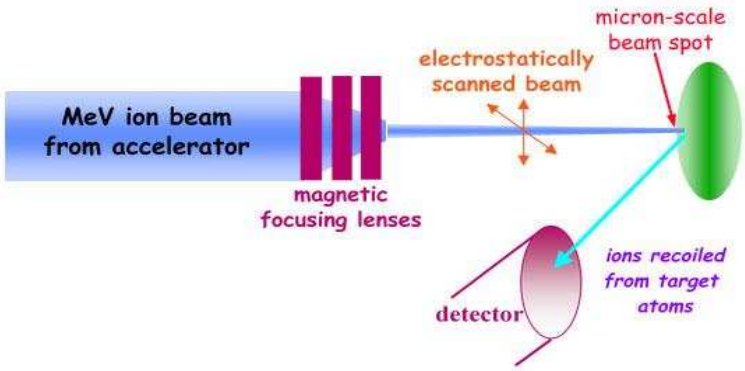

Figure 3.9: Setup for RBS measurement.

collided with and the position of this atom in the sample. For example when the α particle collides with a surface atom the energy of the reflected particle depends on the recoil (weight) of the atom. If the atom is heavier the ion will loose less energy during collision. If the ion enters the sample it will slow down because of the charges that are present. After collision with a sample atom it also has to travel back through the sample to be detected. Consequently it has a lower energy when detected compared to the α-particles which are scattered by the surface atoms. The energy difference between the surface and the bottom of the layer is a measure for the thickness of the sample. Figure 3.10 shows the RBS spectrum of a Al/Py bilayer. The

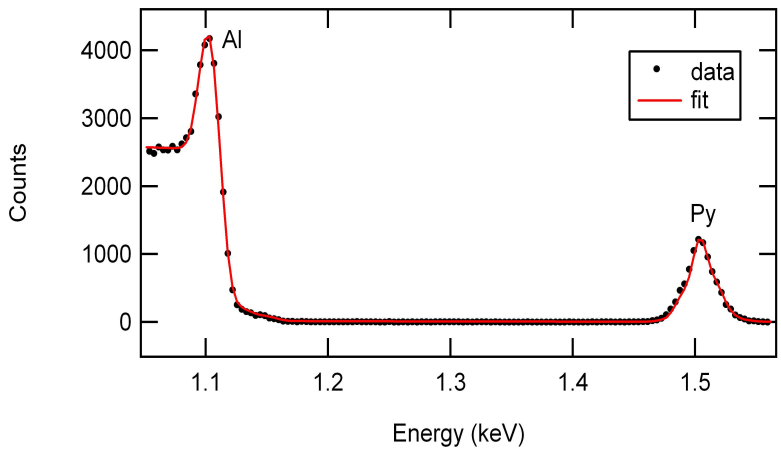

Figure 3.10: spectrum of a RBS measurement.

peak at lower energies is characteristic for the Al layer and the peak at 1.5 keV is the one characteristic for the Py layer. The latter, however, is shifted

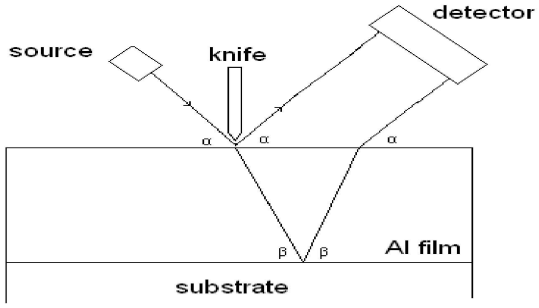

Figure 3.11: Setup for X-ray reflectometry.

to lower energy in comparison with a single Py layer. This is caused by the presence of the Al layer, slowing the α particles down. Therefore, the energy over which the Py peak has shifted is also a measure for the thickness of the Al layer.

3.4.2 X-ray measurements

To confirm the RBS measurements also some X-ray measurements have been performed. However, these films were sputtered on $SrTiO_3$ (STO) substrates because Si substrates are almost equal in electron density as aluminum and therefore unsuitable for X-ray measurements. In figure 3.11 a simple representation of the X-ray measurement setup is given. The detector measures the intensity of the reflected photons. When the angle of incidence α increases the intensity of the reflected photons decreases rapidly over 5-6 orders of magnitude. The photons will be partially reflected on the Al surface but some photons will go through the Al layer and reflect upon the substrate. The different paths taken by the photons have different lengths causing constructive or destructive interference. This causes the so called Kiessig fringes. The spacing between subsequent fringes is dependent on the thickness of the film. To prevent fringes due to spreading of the X-ray beam a knife is placed, so only rays which are reflected directly below the edge of the knife will end up in the detector.

However, there where no fringes visible for the measurements on Al making it very difficult to determine the thickness. This is caused by the roughness of the Al films ($\sim$10 nm) (see section 4.2.2). In the next section the results of the thickness calibration of the aluminum and permalloy target are given.

3.4.3 Conclusion: RBS and X-ray measurements

When films are sputtered the thicknesses of the films need to be verified accurately. The results of the RBS data together with the results of the X-ray measurements are given in tables 3.1 and 3.2. From this we get the

d_{Xtal} (1 nm$\|_{Xtal}$=0.25 nm)	d (RBS and X-ray data)
125 $\dot{A}$	21 nm
250 $\dot{A}$	42 nm
375 $\dot{A}$	62 nm
500 $\dot{A}$	83 nm

Table 3.1: Calibration of the aluminum target

new calibration, 1 nm$\|_{Xtal}$ =0.63 ($\pm$ 0.015) nm. Which means that when the Xtal crystal in the UHV system measures 0.63 ($\pm$ 0.015) nm, the film on the substrate has a thickness of 1 nm.

sputter time	d_{Xtal}	d (X-ray data)
3 min	92 $\dot{A}$	34.5 nm
6 min	181 $\dot{A}$	69.6 nm

Table 3.2: Calibration of the permalloy target

The calibration of the new Py target at an argon pressure of 4 μbar is 1 nm = 2.54 $\dot{A}$. For Py it was much easier to determine the thickness from the X-ray measurements because there were clear Kiessig fringes in the data.

Chapter 4

Results

4.1 Al films: dependence of T_c on thickness of the films.

First single Al layers were measured (4-point measurement) with the LR bridge (see section 3.2). The results are presented in fig 4.1. The graph shows the resistance dependence on temperature of Al thin films of different thicknesses. All films undergo a phase transition from the normal state to the superconducting state. The temperature at which this phase transition occurs, the superconducting transition temperature T_c, decreases when the thickness of the film increases. From these results one can extract not only

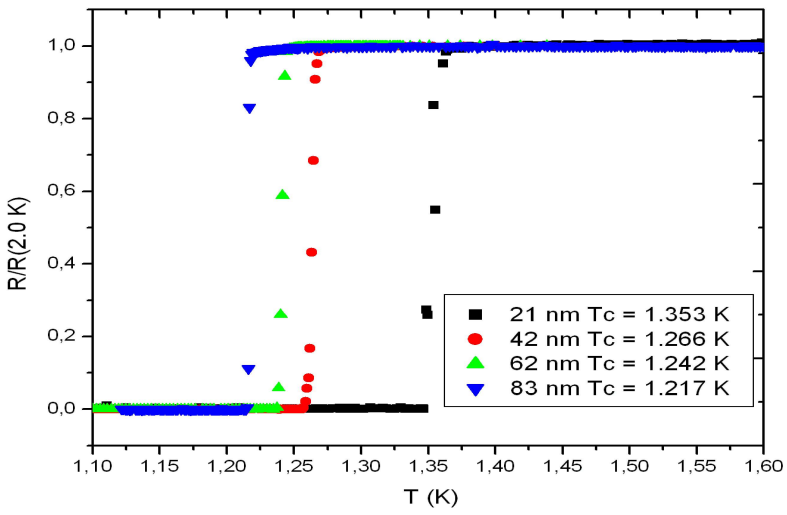

Figure 4.1: Resistance vs. temperature for Al films of various thicknesses.

the T_c, but also the residual resistivity, ρ_0, the residual resistance ratio, RRR, the electronic mean free path, l_e and the BCS and GL coherence lengths ξ_0 and ξ_{GL}. The characteristic values for our Al films are given in table 4.1. The first three columns present the dimensions (d: thickness, w: width, L: length) of the measured films and the third contains the superconducting transition temperature T_c, which can be directly obtained from fig. 4.1. The residual resistivity, ρ_0, can be calculated by extrapolating the normal state resistivity to T=0. The residual resistance ratio is the ratio, $\frac{R(300K)}{R(4.2K)}$, of resistance at room temperature and resistance at 4.2 K. The electronic mean free path can be calculated with eq. 4.1 using N(0) the density of states (DOS) at the Fermi energy, N(0)=$2.2 \cdot 10^{47}$ $J^{-1}m^{-3}$.

$$l_e = \frac{3D}{v_F} \quad \text{with} \quad D = \frac{1}{N(0)e^2\rho_0} \tag{4.1}$$

with D the diffusion coefficient and e the electronic charge. The BCS coherence length is calculated from,

$$\xi_0 = \frac{\hbar v_F}{\pi \Delta(0)} \quad \text{with} \quad \Delta(0) = 1.764 k_B T_c \tag{4.2}$$

with v_F=$1.3 \cdot 10^6$ m/s the Fermi velocity and k_b the Boltzmann constant. The GL coherence length is

$$\xi_{GL} = 0.855 \left(\frac{\xi_0 l_e}{1-t} \right)^{1/2} \tag{4.3}$$

with t=T/T_c. In fig. 4.2 the mean free path vs. thickness of the measured

d(nm)	L(mm)	w(μm)	T_c(K)	$\rho_0(10^{-8}\Omega m)$	RRR	l_e(nm)	$\xi_0(\mu m)$	ξ_{GL}(nm)
21	1.4	200	1.353	3.24	2.12	12.6	1.32	110
42	1.0	5.5	1.266	1.40	3.06	29.1	1.42	171
62	1.0	5.5	1.242	1.26	3.29	32.5	1.44	185
83	1.4	200	1.217	1.12	4.18	36.6	1.47	196
380	1.4	200	–	0.86	5.29	47.4	1.45	223
475	1.4	200	1.237	2.53	2.62	16.2	1.45	130

Table 4.1: Measured in ^{3}He.

Al layers is shown. The mean free path increases for increasing film thickness. The figure clearly shows that the mean free path saturates at a value around 45 nm. The figure also shows that when the thickness is decreased to below the coherence length the interfaces of the film limit the mean free path.

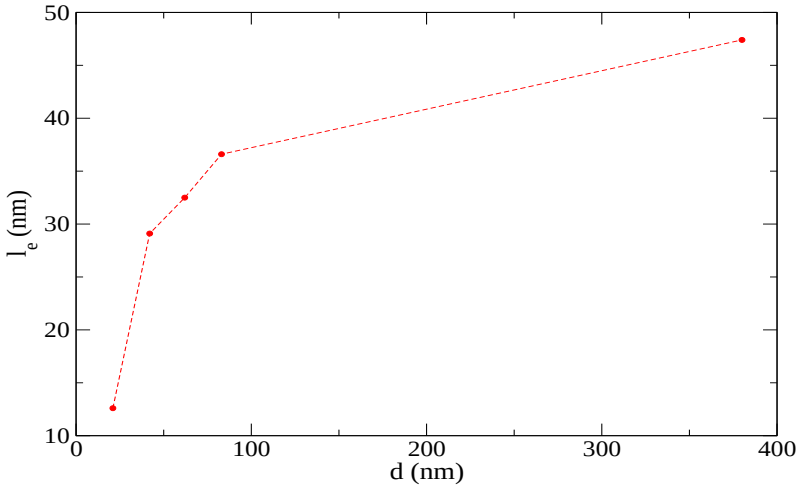

Figure 4.2: Mean free path, l_e, vs. thickness, d, of the Al films .

Furthermore, l_e is a measure of disorder. When the disorder of the material is decreased, the electrons scatter less, resulting in a larger mean free path. The mean free path increases with decreasing disorder and therefore the superconducting transition temperature, T_c, increases with increasing disorder.

4.2 T_c dependence on disorder.

Increasing the amount of disorder in thin superconducting film can induce a change in the transition temperature T_c. The induced change in T_c depends on the structure of the density of states (DOS) near the Fermi energy, since the phonon mediated electron-electron interaction takes place around E_F. There are two different mechanisms which can explain the behavior of T_c with disorder. The change in T_c can be induced by either lattice imperfections or grains.

4.2.1 Imperfections

Lattice imperfections can induce degradation as well as enhancement of the energy gap (T_c) [19]. Typically, T_c degradation is explained as a density of states effect. The metals which exhibit degradation generally have sharp structures in their DOS and have a large N(0) (the DOS at the Fermi energy). Due to scattering these sharp structures around E_F become smeared, reducing N(0) and thereby T_c.

However, Al displays enhancement of T_c with increasing disorder so another explanation is needed. Enhancement generally occurs in metals with a small value of N(0) and a DOS without sharp structures. Imperfections influence the shape of $\alpha^2F(\omega)$, the effective phonon density of states with α the frequency dependent electron-phonon coupling strength. The enhancement is caused by the increased coupling of the electrons to the phonons. There are basically two types of phonons, transverse phonons and longitudinal phonons [20]. In the presence of imperfections two effects occur. The coupling to transverse phonons is increased and the coupling to longitudinal phonons is decreased. However, the first effect is dominant. The coupling to transverse phonons is caused by the fact that the lattice defects allow partial violation of the conservation of momentum during the electron-phonon collisions. This increases $\alpha^2F(\omega)$ in the low frequency regime, making more phonon states available for the phonon mediated electron-electron interaction. Increase of e-ph coupling results in an increase of the energy gap and consequently enhancement of T_c. The second effect can be explained as follows, the electrons fluctuate in phase with the longitudinal phonons creating regions where the electron gas is compressed (electronic mean energy increased) and regions with less electrons (lower mean energy). Electrons diffuse from the dense regions to the less dense regions to compensate the gradient in mean energy and the energy of the phonon dissipates. However, when imperfections are involved the diffusion is partially inhibited and energy cannot be carried away from the phonon therefore increasing the lifetime of the longitudinal phonon and thus decreasing the coupling of the electron to this phonon. The enhanced coupling to transverse phonons is therefore partially canceled by the decrease in coupling to the longitudinal phonons. The dependence of T_c on the mean free path l_e has been derived by Keck and Schmid[20],

$$\frac{T_c - T_c^p}{T_c^p} = \frac{\left(\frac{12}{\pi}\right)\left(\frac{c_L}{c_T}\right)^2 - \left[\left(\frac{8}{\pi}\right) - \left(\frac{\pi}{2}\right)\right]}{\left(\frac{g_L^2 N_0 q_D^2}{4p_0^2}\right)} \frac{1}{q_D l_e} \tag{4.4}$$

They found that the transition temperature increases linearly with l_e^{-1}. With T_c^p the T_c of a pure superconductor (for Al T_c^p=1.16 K [19]), p_0 the momentum at the Fermi energy and c_L and c_T are the longitudinal and transverse sound velocities. Here $q_D = \frac{\Theta_L}{c_L}\frac{k_b}{\hbar}$ (a factor of $\frac{k_b}{\hbar}$ is added to make sure that the dimensions are correct) with Θ_L the Debye temperature. Also present in eq. 4.4 is g_L which is given by

$$g_L = \hbar \frac{p_0^2}{3m\rho^{1/2}c_L} \tag{4.5}$$

the multiplication with $\hbar$ is needed to obtain the correct dimensions. Furthermore, λ_p is a dimensionless coupling constant which is a measure for the

coupling strength of the electrons to the phonons and is given by

$$\lambda_p = \left(\frac{N_0 q_D^2}{4p_0^2}\right) g_L. \tag{4.6}$$

The coupling constant can be estimated for our aluminum. To estimate λ_p the following values were used,

- N_0, the electronic density of states at the Fermi energy per spin, is $1.1{\cdot}10^{47}$ J^{-1} m^{-1}[26].
- q_D, the phonon wave vector, is $1.32{\cdot}10^{10}$ m^{-1}[26].
- $p_0{=}\hbar k_F$ with $k_F{=}1.75{\cdot}10^{10}$ m^{-1} the wave vector at E_F[26].
- m, the electronic mass, is $9.1{\cdot}10^{-31}$ kg.
- ρ, the ionic mass density, is $2.7{\cdot}10^3$ kg m^{-3}.
- Θ_L, the Debye temperature, is 394 K.
- k_B, the Boltzmann constant, is $1.38{\cdot}10^{-23}$ J K^{-1}.
- $\left(\frac{c_L}{c_T}\right)$=4.13.

Using the values above results in a coupling constant of the order of 0.5-0.6. This coupling constant induces a change of T_c, compared to T_c^p of pure aluminum, of the order of 70 mK (for the 62 nm film) which is in good agreement with our results (see table 4.1). In figure 4.3 the T_c dependence on the mean free path, l_e, of our aluminum films is presented. The graph shows a linear increase of T_c with l_e^{-1} for the films with thicknesses 42 nm-83 nm (the results for the 21 nm film seems to deviate). Another form of a lattice defect that influences the energy gap is a grain boundary which exists in polycrystalline Al.

4.2.2 Single crystalline or granular films?

The growth process of the films determines whether they will become single crystalline or polycrystalline (i.e. granular). For single crystalline films Fortuin [21] found a T_c between 1.10 K and 1.15 K for varying line widths (0.04 and 0.14 μm and thicknesses of 20 and 100 nm). However, our films have a T_c around 1.26 K (21 nm) and the lowest T_c was 1.217 K for the 83 nm film. Obviously our films are polycrystalline,which was confirmed by AFM measurements shown in figures 4.4 and 4.5. The boundaries of the grains (surface grains: 50-100 nm) influence the superconducting properties such as T_c. This change in T_c is caused by the following two competing effects:

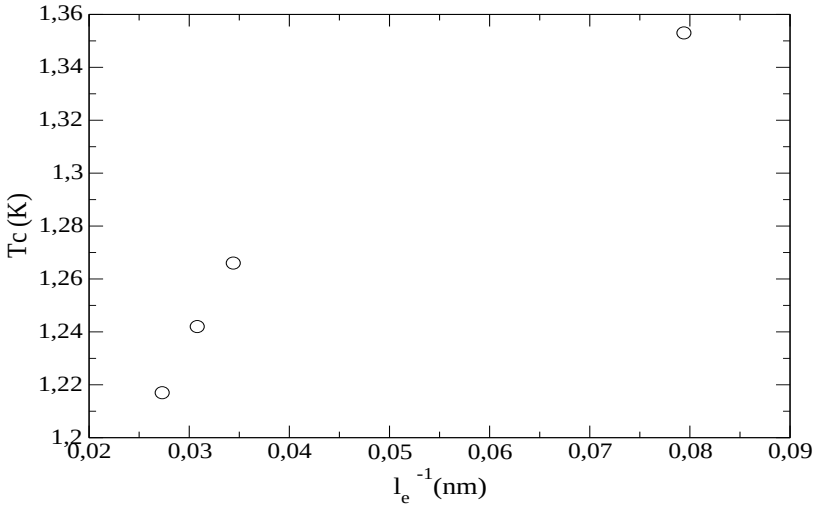

Figure 4.3: T_c vs. l_e^{-1} for the aluminum films (see fig. 4.1).

- The grain boundaries induce an increase in the average phonon amplitude of the ions. The formation of these boundaries reduces the symmetry of the ions positioned near a grain boundary. Because of this symmetry loss the ions near the boundaries are held in place by weaker ionic forces then in the bulk of the crystal. Therefore, they can vibrate with larger amplitude and lower frequency then the bulk ions. The average phonon amplitude will therefore be enhanced and as a result T_c will increase when the film becomes polycrystalline[22].

- The introduction of grain boundaries (i.e. disorder) makes more vibrational states available through scattering. This has a broadening effect on the phonon density of states. This effect will suppress T_c instead of enhancing it.

Since in our case we have T_c enhancement compared to the single crystalline Al films of Fortuin, apparently the first effect is more important than the second. The amount of T_c enhancement depends on the size of the grains.

T_c dependence on grain size.

The transition temperature in bulk superconductors lies considerably lower than the T_c of superconducting particle (i.e. grain). When an electron is trapped in a box (grain) its energy spectrum will become discrete. These discrete energy levels are raised when the dimensions of the box are decreased.

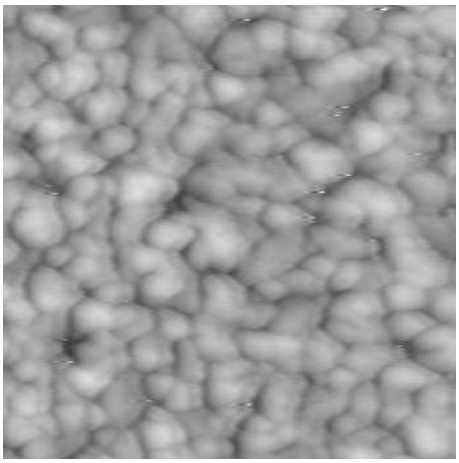

Figure 4.4: Topology of the surface of the Al layer on a Si substrate. Thickness of film: 62 nm. Roughness: ∼10 nm. Grain size (surface grains): 50-100 nm.

Therefore, a polycrystalline film has elevated energy levels compared to the single crystalline films. This explains the increase in T_c when superconducting film is more granular.

In subsection 4.2.1 a mechanism was presented to explain the enhancement of T_c with disorder. However, one might imagine a second mechanism to be responsible for the change in T_c with disorder. Namely, a decrease in the size of the grain when the strain on the grain is increased. Due to lattice mismatch between the Si-substrate and the Al film, the Al film is under strain. This strain relaxes with increasing thickness of the film. Therefore one can imagine that the size of the grain will increase with film thickness, which could explain the induced decrease in T_c with increasing film thickness. However, the T_c of the single crystalline films of Fortuin is also enhanced with disorder. Therefore the grains are not responsible for the T_c enhancement with decreasing film thickness, only for the enhancement compared to single crystalline films.

Parmenter[23] derived the following equation for T_c enhancement with grainsize.

$$\frac{T_c}{T_{c\infty}} ln \frac{T_c}{T_{c\infty}} = \frac{1}{2}\pi (L/a)^3 (C/4) \tag{4.7}$$

with $T_{c\infty}$ the bulk superconducting transition temperature, $L \equiv (\lambda_F^2 \xi_0)^{1/3}$ where λ_f is the Fermi wavelength, a is the grain size, $C \equiv \Delta(0)/k_B T_c = 3.528$ and $\xi_0 = 0.15(\hbar v_F / k_b T_c)$ the Pippard coherence length. The T_c of our polycrystalline film is 1.217 K (d=83 nm) and the T_c of bulk aluminum is 1.16 K [19]. When this is put in equation 4.7 one can calculate the size of the grains in our films. For Al L∼6.2 nm and thus the grainsize which induces a T_c enhancement of 0.05 K is a ∼20 nm. The surface grains are

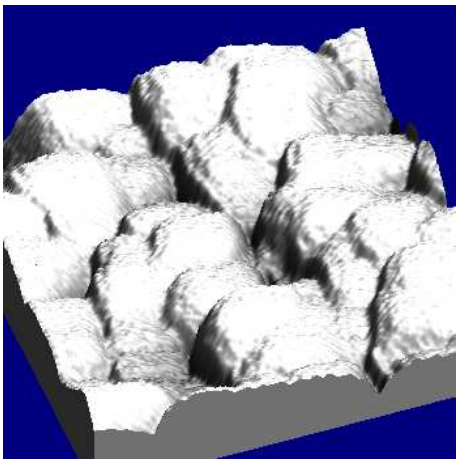

Figure 4.5: Topology of the surface of the Al/Py bilayer on a Si substrate.

50-100 nm. Maybe, the size of the grains inside the sample can be much smaller than the surface grains and are of the order of 20 nm.

4.3 Al: type I or type II superconductor?

As discussed in chapter 2, superconductors can be divided into two groups. In the first superconductivity is destroyed at a certain critical field. The other contains superconductors in which regions of normal state nucleate at a certain critical field and superconductivity is destroyed at a second larger magnetic field. Superconductors are categorized by using their value for κ,

$$\kappa = \frac{\lambda_L(T)}{\xi(T)} \tag{4.8}$$

The following equation was used to calculate the bulk penetration depth,

$$\lambda = \lambda_L(0)\sqrt{\frac{\xi_0}{l_e}} \tag{4.9}$$

and when the film is much thinner than the bulk penetration depth,

$$\lambda_\perp = \frac{\lambda^2}{d} \tag{4.10}$$

should be used. The values for ξ, l_e, d and ξ_0 can be found in table 4.1. When $\kappa < \frac{1}{\sqrt{2}}$ the superconductor is of type I and when $\kappa > \frac{1}{\sqrt{2}}$ it is of type II. Apparently, the very thin films are of type II while the thick film is of type I. The aluminum which is to be used in the lateral spin switch has a thickness of 80 nm and will be a type I superconductor with only one critical magnetic field. The value for κ is given in table 4.2. Here $\lambda_L(0)$=16 nm [24] was used.

d (nm))	λ (nm)	$\lambda_\perp$ (μm)	κ	type
21 nm	163.7	1.27	11.6	II
42 nm	111.7	0.297	1.74	II
62 nm	106.5	0.183	0.99	II
83 nm	101.4	0.124	0.63	I

Table 4.2: Characteristic values of our Al for the bulk penetration depth, $\lambda_\perp$ and κ.

4.4 Py film: AMR measurement and simulations.

Besides the single layers of Al there was also an AMR measurement performed on a Py strip. The spin of an electron can affect the transport of the electron. The AMR (anisotropic magnetoresistance) is an example, here the resistance of a ferromagnet is dependent on the angle between the magnetization and the current direction. The AMR is therefore a measure for the anisotropy and domain structure of the ferromagnet. When the ferromagnet has a preferred magnetization direction in the demagnetized state, an applied field along that direction will not induce a resistance difference. When the field is applied perpendicular to the axis of easy magnetization there is a change in resistance when the direction of magnetization is changed. When the magnetization direction is perpendicular to the current direction the resistance of the ferromagnet is smaller than for the case were the magnetization is parallel to the current. In literature a difference in resistance of 3-4 percent is given for permalloy. In figure 4.7 an AMR measurement is shown of a Py strip[1] with a width of 1.5 μm (see fig 4.6). As can be seen from figure 4.6 the resolution is considerably improved by sputtering at a lower argon pressure (2 μbar) compared to the structure in fig. 3.6 (sputtered at 4 μbar). A resistance difference of about 2.7 percent is measured which is in reasonable agreement with literature.

To investigate the switching fields of different sizes of Py strips simulations were performed using the OOMMF code[25]. When a magnetic field is applied over a ferromagnet a torque, $\mathbf{L}$, is exerted on the moments of magnetization (spins) resulting in rotation of the spins. The torque tends to bring the system back to equilibrium which is disturbed by the applied field. In equilibrium the torque must be equal to zero. The equation of motion for the magnetization $\mathbf{M}$ is,

$$\frac{d\mathbf{M}}{dt} = \gamma_0 \mathbf{L} \quad \text{and} \quad \mathbf{L} = \mathbf{M}\text{x}\mathbf{H} \tag{4.11}$$

with γ_0 the gyromagnetic ratio and $\mathbf{H}$ an effective magnetic field. However, in the above equation dissipation has not been taken into account. With a

[1]The sample was fabricated by Marcel Hesselberth: argon pressure of 2 μbar.

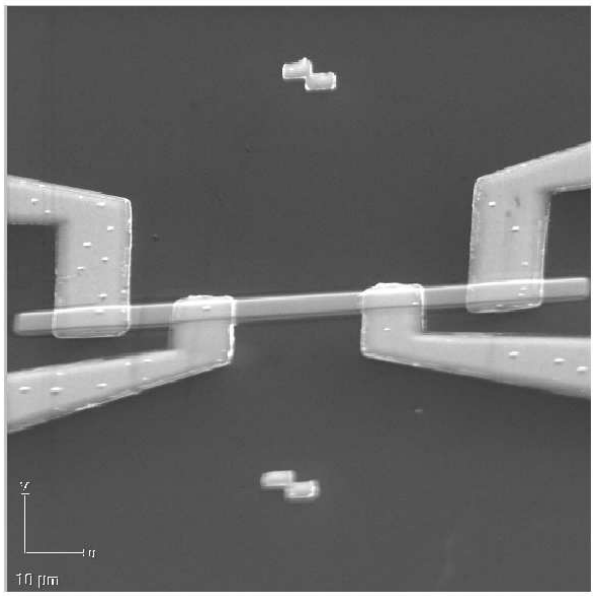

Figure 4.6: Py strip with dimensions: w=1.5μm, l=20μm and t=40nm.

dissipative term added the equation becomes,

$$\frac{d\mathbf{M}}{dt} = -\gamma_0^{'}\mathbf{M}\mathrm{x}\mathbf{H} - \frac{\gamma_0^{'}\alpha}{M_s}\mathbf{M}\mathrm{x}\mathbf{M}\mathrm{x}\mathbf{H} \tag{4.12}$$

with $\gamma_0^{'}$ the Landau-Lifshitz gyromagnetic ratio, α the damping coefficient and M_s the saturation magnetization. The integration of this equation of motion results in a hysteresis loop. This loop was simulated for several widths of the ferromagnetic strip keeping the thickness (40 nm) and the length (10 μm) constant. For the damping coefficient we kept the default value of 0.5, the magnetocrystalline anisotropy, K_1 was taken to be equal to zero, for the exchange constant, A, the default value, $13{\cdot}10^{-12}$ J/m was used and the saturation magnetization was taken to be 800 10^3 A/m. The coercive fields which are extracted from the hysteresis loops are plotted versus the width of the simulated strip (see fig. 4.8). Using fig. 4.8 the width of the Py electrodes of the lateral spin switch can be chosen. The widths of the electrodes were chosen to be 1.5 μm and 300 nm. The graph in fig. 4.8 shows a significant difference in switching fields for these strips.

4.5 Al/Py bilayers: Suppression of T_c.

To test whether the coherence length of Al is long enough for use in a lateral spin switch, Al/Py bilayers where measured. The results are given in Figure 4.9. Suppression of T_c occurs when the thickness of the superconducting

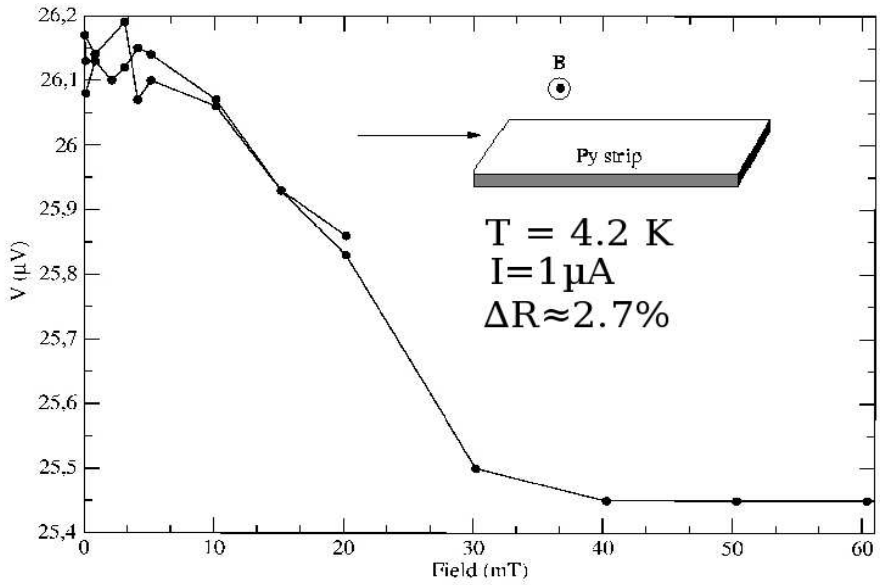

Figure 4.7: AMR measurement of a Py layer.

Dimensions: (d=40 nm x l=10 um x w)

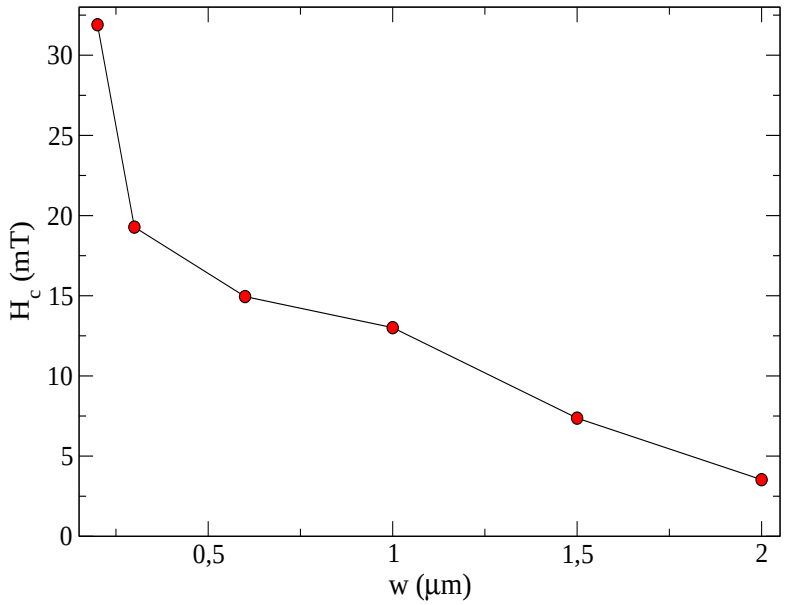

Figure 4.8: Coercive field H_c vs. width of Py strips simulated with OOMMF.

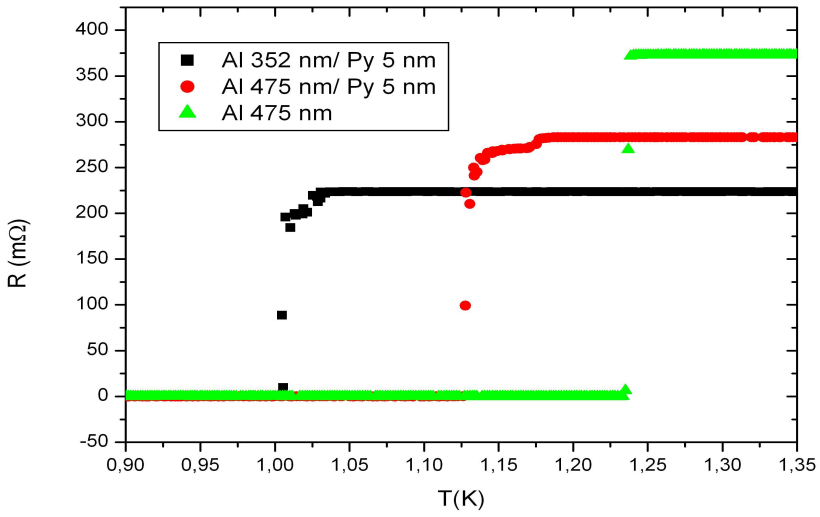

Figure 4.9: Suppression of T_c due to proximity of a Py layer.

layer is of the order of twice the superconducting coherence length, ξ_s. The figure shows a single Al layer (green curve) of 475 nm and two Al/Py layers (red curve 475 nm/5 nm and black curve 352 nm/5 nm). The T_c of the single layer of Al is 1.237 K, the bilayer with the same thickness for Al layer but with 5nm of Py underneath has a T_c of 1.13 K and thus shows some suppression. The curve of the 352 nm Al layer with also 5nm of Py underneath has a T_c of around 1.0 K. This T_c is definitely not reachable by increasing the thickness of the Al layer (bulk value: T_c=1.18 K). At a thickness 350 nm there already is considerable suppression which is in good agreement with the coherence length of our aluminum (see table 4.1). This test shows that Al has a coherence length which is long enough for usage in lateral spin switches. In section 2.7 the suppression of T_c of a bilayer, as function of the thickness of the superconducting layer, was derived.

$$T_c = T_{c0} - \frac{\pi^2 \xi_{GL}^2}{d^2} \tag{4.13}$$

with d the thickness of the superconducting layer. With eq. 4.13 the Ginzburg Landau coherence length (of the unperturbed aluminum layer) can be calculated using the information obtained from figure 4.9. This calculation results in a coherence length of 155 nm for the 475 nm Al layer. This is in reasonable agreement with the coherence length in table 4.1.

For the bilayers the graph shows a step in the transition from normal to superconducting state. Apparently, there are regions in the Al layer where T_c is more suppressed than in other parts of the layer. The explanation of

this effect may come from the fact that the Py film has multiple domains. It has been shown by Rusanov[17] that S/F bilayers where F has multiple domains shows the same effect as a spin switch. In a spin switch (F/S/F geometry) Cooper pairs probe both F layers, hence, a Cooper pair can also probe both magnetization directions on either side of a domain wall causing the same effect. In some parts of the Al layer the Cooper pairs probe domains with nearly parallel magnetization direction while in other parts they probe nearly antiparallel configurations. Therefore in some regions in the superconductor T_c is suppressed more than in other regions. This also explains the "sharpness" of the step. Thickness gradients could also cause suppression of T_c in some thinner regions of the sample but this effect can be ruled out because this would cause a more gradual decrease in resistance.

Chapter 5

Conclusions

In this project it was tested if fabrication and measurement of a lateral spin switch is possible. Single layers were measured to characterize the Al. The T_c dependence on disorder seems to be caused by the enhancement of electron-phonon coupling due to lattice imperfections. From measuring the single Al layers and the Al/Py bilayers the conclusion can be drawn that aluminum is suitable for usage in a lateral spin switch. We find that the coherence length is long enough (ξ_0=1.47 μm, ξ_{GL}=196 nm). According to the simulations (see fig. 4.8) it is also possible to fabricate Py electrodes with different switching fields. Therefore we can conclude that it is possible to fabricate a lateral spin switch. However, the fabrication process requires accurate choice of parameters, therefore dose tests for different resist thicknesses were performed resulting in the parameters given in Appendix C. Also the argon pressure during sputtering is a critical parameter, for Py sputtering at 2 μbar (instead of 4 μbar) improves the resolution enormously. As mentioned in chapter 6 the roughness of the Al greatly impedes the ability to calibrate the thickness of the Al layers. The roughness can be decreased also by decreasing the argon pressure (shown by others in the group) but another solution would be to change the sputtering process into an evaporation process. This will also solve the resolution and definition problems caused by sputtering.

However, the fabrication process is now known to us and we have confirmed that Al would be an excellent candidate for the superconducting structure in the lateral spin switch. In the future a F/S/F lateral spin switch could be measured.

Appendix A

Calibration of 2 kΩ RuO_2 thermometer.

Figure A.1 shows the calibration of RuO_2 thermometer. Red symbols: Temperature vs. Resistance measured in the ^{3}He cryostat (section 3.1) and the black symbols is a fit to the red curve. The green and blue curve where measured in the dilution fridge. The table contains the values of the dilution fridge measurement. The measurements of the dilution fridge are in excellent agreement with the measurement of the ^{3}He cryostat (the resistor used here was not the same as the one used in the dilution fridge however, they did come from the same batch).

Calibration Table: 2 kΩ RuO_2 resistor

R_2K RuO_2 (kΩ)	T(K)	T_{Fit}(K)
24.2956	0.0495	0.0500
24.1747	0.0505	0.0504
21.1880	0.0622	0.0618
19.5796	0.0696	0.0700
19.2268	0.0718	0.0720
17.3140	0.0844	0.0852
16.3572	0.0934	0.0934
15.9393	0.0981	0.0974
15.0481	0.1073	0.1070
14.8067	0.1108	0.1099
13.7753	0.1245	0.1239
13.2070	0.1337	0.1329
12.8643	0.1399	0.1389
12.6435	0.1443	0.1431
12.3598	0.1497	0.1487
11.9491	0.1586	0.1575
11.1344	0.1791	0.1779
10.7392	0.1919	0.1895
9.9404	0.2158	0.2172
9.3849	0.2383	0.2407
9.0404	0.2531	0.2576
8.8497	0.2651	0.2678
8.5280	0.2838	0.2867
8.1860	0.3057	0.3094
7.8835	0.3288	0.3321
7.6440	0.3502	0.3521
7.4123	0.3708	0.3735
7.2575	0.3872	0.3890
7.0777	0.4076	0.4085
6.9416	0.4229	0.4244
6.7427	0.4504	0.4495
6.5746	0.4723	0.4727
6.3767	0.5030	0.5028
6.2601	0.5227	0.5221
5.9631	0.5786	0.5773

6.0889	0.5549	0.5528
5.8417	0.6043	0.6027
5.6801	0.6466	0.6396
5.4923	0.6945	0.6876
5.2986	0.7504	0.7437
5.2391	0.7691	0.7626
5.0391	0.8365	0.8321
4.9132	0.8849	0.8816
4.7900	0.9381	0.9351
4.6808	0.9891	0.9872
4.5221	1.0681	1.0722
4.4578	1.1047	1.1102
4.3809	1.1517	1.1588
3.7951	1.6875	1.6884
3.6507	1.8762	1.8851

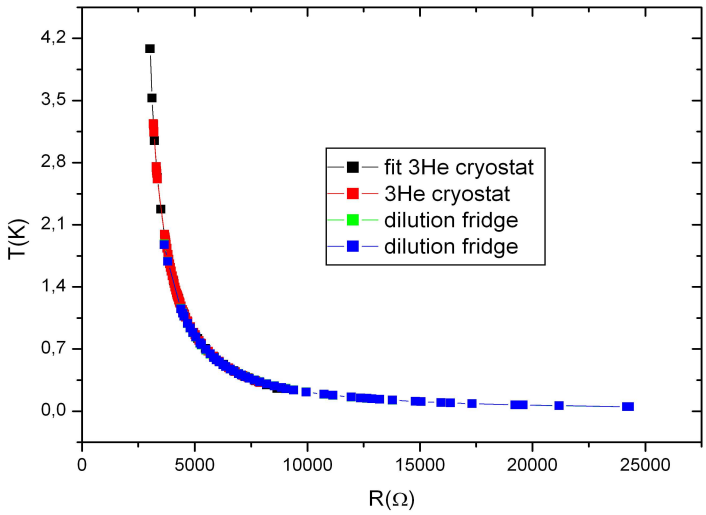

Figure A.1: Calibration of a 2 kΩ RuO_2 thermometer.

Appendix B

Calibration coil.

In the figure below the "home made" coil is shown. The coil was made of

Figure B.1: Home made coil.

superconducting wire (NbTi with Cu filaments). The wire thickness is 0.12 μm and the coil has 1886 windings (2 layers). At 1 Tesla the critical current is 6.7 A. In the graph (fig. B.2) below the calibration of the coil is shown. The calibration was done with a Hall probe. The Hall probe was calibrated in the PPMS and the results are shown in fig. B.3.

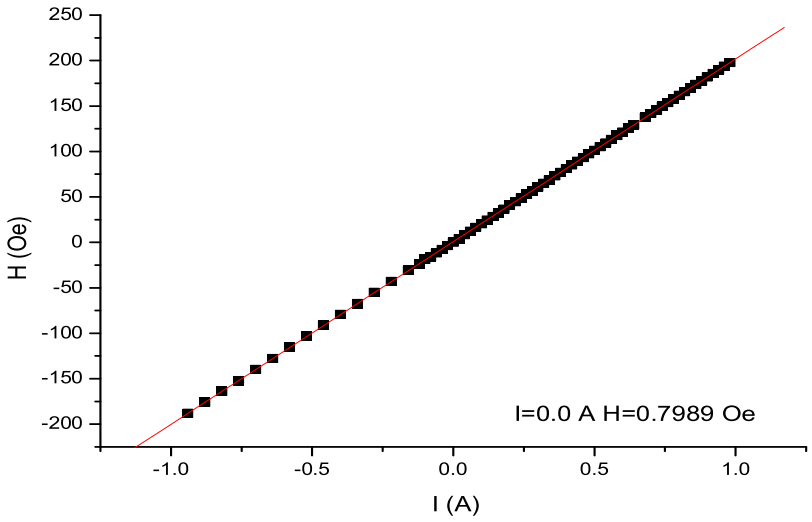

Figure B.2: Calibration of the coil: magnetic field vs. current.

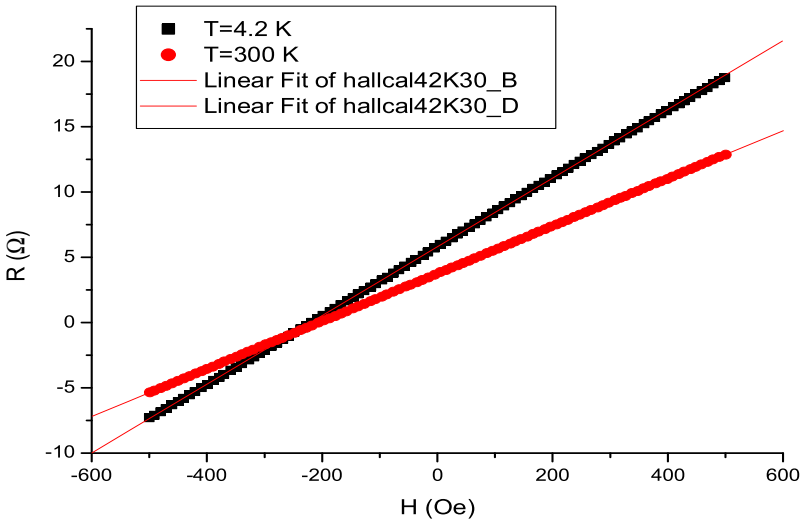

Figure B.3: Calibration of Hall probe: resistance vs. applied magnetic field at 300 K(red) and 4.2K(black).

Appendix C

Process parameters for the fabrication of the lateral spin switch using the lift-off technique.

C.1 Py:

Spincoat PMGI SF 3.6 4000 rpm
ramp1: 2 s
ramp2: 1 s
time: 50 sec
thickness: 100 nm
Bake 30 min 190 °C

Spincoat PMMA A2 4000 rpm
ramp1: 2 s
ramp2: 4 s
time: 50 sec
thickness: 60 nm
Bake 60 min 140 °C

Exposure parameters:
I=50 pA
Area Dose= 160 μAs cm^2
Dose factor=2.3
The small structures (small strip and alignment markers) were exposed with relative dose 1.2 while the large strip and large alignment markers were exposed with a relative dose of 1.0.

Development:
PMMA 30 sec MIBK:IPA 1:3 and IPA 1 min rinse and dry
PMGI 2.5 min PMGI developer and H_2O rinse and dry
Post bake: 30 min 140 °C

Sputtering:
UHV
I= 165 mA
P= 4 μbar
thickness: 40 nm

C.2 Al:

Spincoat PMGI SF 5 2300 rpm
ramp1: 2 s
ramp2: 1 s
time: 50 sec
thickness: 200 nm
Bake 30 min 190 °C

Spincoat PMMA A2 4000 rpm
ramp1: 2 s
ramp2: 4 s
time: 50 sec
thickness: 60 nm
Bake 60 min 140 °C

Exposure parameters:
I=50 pA
Area Dose= 160 μAs cm^2
Dose factor=2.3

Development:
PMMA 30 sec MIBK:IPA 1:3 and IPA 1 min rinse and dry
PMGI 3 min PMGI developer and H_2O rinse and dry
Post bake: 30 min 140 °C

Sputtering:
UHV
I= 220 mA
P= 6 μbar
thickness: 80 nm

C.3 Au:

Spincoat PMMA A2 6000 rpm
ramp1: 2 s
ramp2: 1 s
time: 50 sec
thickness: 60 nm
Bake 60 min 140 °C

Exposure parameters:
I=50 pA
Area Dose= 140 μAs cm^2
Dose factor=2.0

Development:
PMMA 30 sec MIBK:IPA 1:3 and IPA 1 min rinse and dry
Post bake: 30 min 140°C

Sputtering:
Z-400:
P=4.9 10^{-6} mbar
MoGe 20 sec (adhesion layer)
Au 200 sec

Bibliography

[1] J. Bardeen, L.N. Cooper and J.R. Schrieffer, Phys. Rev. **108**, 1175 (1957).

[2] V.L. Ginzburg and L.D. Landau, Zh. Eksperim. i Teor. Fiz. **20**, 1064 (1950).

[3] L.R. Tagirov Phys. Rev. Lett. **83**, 2058 (1999).

[4] A.I. Buzdin, A.V. Vedyayev and N.V. Ryzhanova, Europhysics Letters, **48**, 686 (1999)

[5] I. Baladié, A. Buzdin, A. Vedyayev and N. Ryzhanova, Phys. Rev. B, **63**, 054518 (2001)

[6] J.Y. Gu et al. Phys. Rev. Lett. **89**, 267001 (2002).

[7] W. Meisner and R. Ochsenfeld, Naturwissenschaften **21**, 787 (1933).

[8] F. and H. London, Proc. Roy. Soc. (London) **A149**, 71 (1935).

[9] J.G.Daunt and K. Mendelssohn, Proc. Roy. Soc. (London) **A185**, 225 (1946).

[10] J. Bardeen "Theory of superconductivity" in S. Flgge (ed.) Handbuch der Physik vol. XV Springer Verlag, Berlin (1956).

[11] J. Zaanen, The classical condensates, Lorentz Institute of Theoretical Physics, University of Leiden, 1996.

[12] M. Tinkham, Introduction to superconductivity, McGraw-Hill, Inc. p.53 eq. 3.20 (1996).

[13] M. Tinkham, Introduction to superconductivity, McGraw-Hill, Inc. p.111 eq. 4.1 (1996).

[14] M. Tinkham, Introduction to superconductivity, McGraw-Hill, Inc. p.120 eq. 4.26a (1996).

[15] A.F. Andreev, Sov. Phys. JETP, **19**, nr. 5, 1228 (1964).

[16] A. Yu. Rusanov, R. Boogaard, M Hesselberth, H. Sellier, J.Aarts Physica C **369** 300 (2002)

[17] A. Yu. Rusanov, M Hesselberth, J.Aarts Phys. Rev. Lett. **93** 057002 (2004)

[18] F. Jedema, Ph.D. thesis "Electrical spin injection in metallic mesoscopic spin valves" (2002).

[19] D. Belitz, Phys. Rev. B, **36**, 47 (1987).

[20] B. Keck, A. Schmid J. Low Temp. Phys. **24**, 611 (1976).

[21] A.W. Fortuin Ph.D. thesis "Superconducting phenomena near the transition temperature in single crystalline Aluminum nanostructures" (1997)

[22] J.W. Garland, K.H. Brennemann, F.M. Mueller, Phys. Rev. Lett. **21**, 1315 (1968)

[23] R.H. Parmenter, Phys. Rev. **166**, 392 (1968).

[24] J. Romijn, T. M. Klapwijk, M.J. Renne, J.E. Mooij, Phys. Rev. B **26** 3648 (1982).

[25] http://math.nist.gov/oommf/

[26] N.W. Ashcroft and N.D. Mermin, Solid state physics, Saunders College Publishing, 1976.

Acknowledgments:

I want to thank the following individuals for their assistance during my graduation project:

- Jan Aarts: head of the MSM group, for his supervision.
- Federica Galli: for her every day supervision and assistance with the experiments.
- Marcel Hesselberth: for technical support and RBS measurements.
- Ruud Hendrikx: for AFM and X-ray measurements.